Article

Cell

Enhanced Dendritic Compartmentalization in Human Cortical Neurons

Graphical Abstract

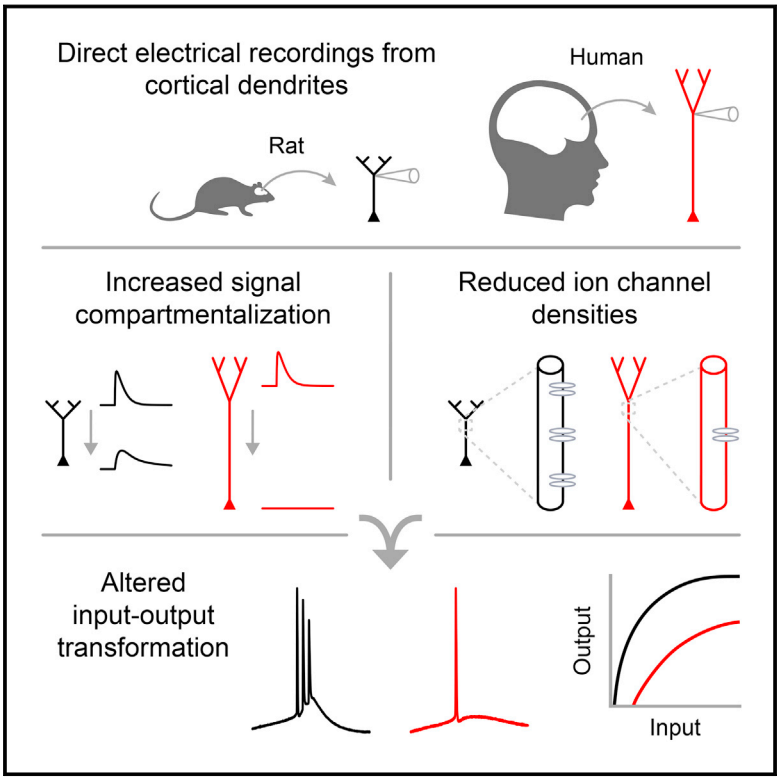

Authors

Lou Beaulieu-Laroche, Enrique H.S. Toloza, Marie-Sophie van der Goes, ..., Matthew P. Frosch, Sydney S. Cash, Mark T. Harnett

Correspondence

scash@mgh.harvard.edu (S.S.C.), harnett@mit.edu (M.T.H.)

In Brief

Human cortical neurons exhibit a higher degree of voltage compartmentalization compared to rodent counterparts due to lower ion channel densities across larger dendritic surfaces.

Highlights

- Direct electrical recordings to compare human and rat cortical dendrites
- Longer human dendrites exhibit increased electrical compartmentalization
- Reduced ion channel densities in human dendrites
- Compartmentalization alters the input-output properties of human neurons

Beaulieu-Laroche et al., 2018, Cell *175*, 643–651
October 18, 2018 Published by Elsevier Inc.
https://doi.org/10.1016/j.cell.2018.08.045

CellPress

Cell

Enhanced Dendritic Compartmentalization in Human Cortical Neurons

Lou Beaulieu-Laroche,[1] Enrique H.S. Toloza,[1] Marie-Sophie van der Goes,[1] Mathieu Lafourcade,[1] Derrick Barnagian,[1] Ziv M. Williams,[2] Emad N. Eskandar,[2] Matthew P. Frosch,[3] Sydney S. Cash,[4,*] and Mark T. Harnett[1,5,*]

[1]McGovern Institute for Brain Research, Department of Brain and Cognitive Sciences, Massachusetts Institute of Technology, Cambridge, MA, USA

[2]Department of Neurosurgery, Massachusetts General Hospital, Boston, MA, USA

[3]C.S. Kubik Laboratory for Neuropathology, Massachusetts General Hospital, Boston, MA, USA

[4]Department of Neurology, Harvard Medical School and Massachusetts General Hospital, Boston, MA, USA

[5]Lead Contact

*Correspondence: scash@mgh.harvard.edu (S.S.C.), harnett@mit.edu (M.T.H.)

https://doi.org/10.1016/j.cell.2018.08.045

SUMMARY

The biophysical features of neurons shape information processing in the brain. Cortical neurons are larger in humans than in other species, but it is unclear how their size affects synaptic integration. Here, we perform direct electrical recordings from human dendrites and report enhanced electrical compartmentalization in layer 5 pyramidal neurons. Compared to rat dendrites, distal human dendrites provide limited excitation to the soma, even in the presence of dendritic spikes. Human somas also exhibit less bursting due to reduced recruitment of dendritic electrogenesis. Finally, we find that decreased ion channel densities result in higher input resistance and underlie the lower coupling of human dendrites. We conclude that the increased length of human neurons alters their input-output properties, which will impact cortical computation.

INTRODUCTION

Human pyramidal neurons possess larger dendritic arbors than rodent and primate neurons (Elston et al., 2001; Mohan et al., 2015), but their input-output properties remain unknown. Dendrites filter synaptic events as they propagate toward the soma (Magee, 2000; Spruston, 2008); however, dendritic spikes can amplify local signals to overcome electrical compartmentalization (Harnett et al., 2013; Larkum et al., 2001, 2009; Larkum and Zhu, 2002; Major et al., 2013; Schiller et al., 1997, 2000; Spruston, 2008; Williams, 2004; Williams and Stuart, 2002). These opposing attributes enable dendritic compartments to perform local operations on their inputs (e.g., coincidence detection). Multiple functionally independent compartments, integrating different streams of information (e.g., feedforward and feedback inputs) (Halgren et al., 2018; Petreanu et al., 2009; Spruston, 2008), could endow individual neurons with the sophistication of small computational networks (Guerguiev et al., 2017; Häusser and Mel, 2003; Jadi et al., 2014; London and Häusser, 2005; Poirazi et al., 2003; Polsky et al., 2004; Tran-Van-Minh et al., 2015).

We reasoned that the increased length of human dendrites could further compartmentalize synaptic integration and information processing within individual neurons. However, because compartmentalization critically relies upon details of membrane properties and active conductances (Atkinson and Williams, 2009; Stuart and Spruston, 1998), which cannot be predicted by anatomical features alone, it is not known to what degree human neurons differ from their non-human counterparts. Here, we employ direct patch-clamp electrophysiology to test the hypothesis that dendritic integration is more functionally segregated in human pyramidal neurons.

RESULTS

Reduced Burst Firing in Human Neurons

We performed whole-cell recordings from layer 5 (L5) pyramidal neurons in acute human brain slices obtained from the anterior temporal lobe of neurosurgical patients (Figure 1A; STAR Methods). Compared to rat temporal association cortex (TEA) (Eyal et al., 2016; Mohan et al., 2015) somas, human somas were less excitable (Figures 1H and 1I). Most rat L5 neurons exhibited high frequency (>150 Hz) bursts of action potentials (APs) with threshold current injections (rheobase), but few human L5 neurons did (Figures 1G and S1). Consistent with previous rodent research (Connors et al., 1982; de Kock and Sakmann, 2008), burst firing was more prevalent in L5 than in L2/3 neurons (Figure S2). Electrical coupling between somatic and dendritic compartments and the recruitment of dendritic voltage-gated channels have been proposed to underlie bursting in rodent L5 pyramidal neurons (Larkum and Zhu, 2002; Mainen and Sejnowski, 1996; Williams and Stuart, 1999). We observed a reduction in AP amplitude and first derivative (dV/dt) in rat L5 bursts (Figures 1C and 1D), indicative of a strong dendritic depolarizing envelope (Williams and Stuart, 1999). These features were not present in the firing patterns of human L5 neurons. Our results suggest that somatic inputs are less likely to engage dendritic electrogenesis eliciting bursting in human L5 neurons.

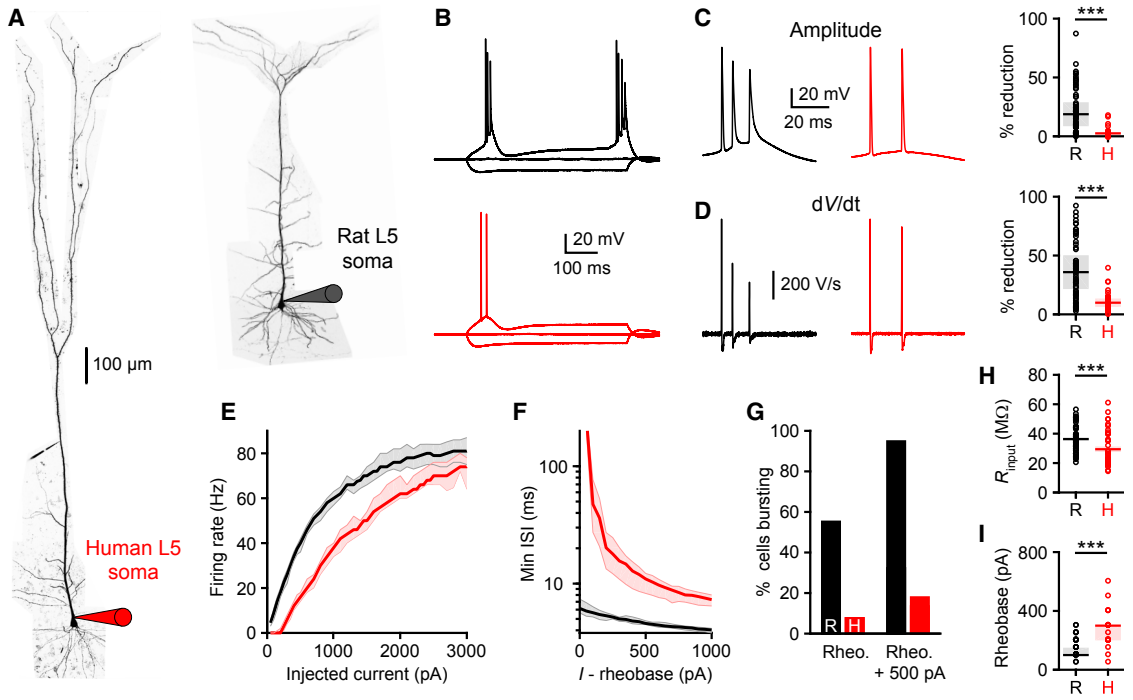

Figure 1. Human Cortical Pyramidal L5 Neurons Exhibit Reduced Burst Firing

(A) Two-photon z stack montage image of human (left) and rat (right) L5 neurons with somatic patch-clamp electrodes.

(B) Rat (black) and human (red) somatic voltage in response to step current injections (−300 pA and rheobase).

(C–I) Somatic properties of L5 neurons (rat: n = 70 recordings from 18 rats; human: n = 39 recordings from 6 patients). (C) Left: APs from (B) expanded to illustrate high-frequency bursting in the rat neuron but not the human neuron. Right: maximal AP amplitude reduction (***$p < 10^{-10}$, Wilcoxon rank sum test). Pooled data represent median and interquartile range. (D) Left: first derivative (d*V*/dt) of voltage waveforms in (C). Right: maximal d*V*/dt reduction (***$p < 10^{-8}$, Wilcoxon rank sum test). Pooled data represent median and interquartile range. (E) Firing rates as a function of injected current. Lines represent population medians with 95% confidence intervals. (F) Minimum instantaneous interspike interval (ISI) as a function of injected current above rheobase. Lines represent population medians with 95% confidence intervals. (G) Percentage of neurons exhibiting bursts (>150 Hz) at rheobase and rheobase + 500 pA. (H) Input resistance (***$p < 10^{-3}$, unpaired t test). Pooled data represent mean ± SEM. (I) Rheobase (***$p < 10^{-11}$, Wilcoxon rank sum test). Pooled data represent median and interquartile range. See also Figures S1 and S2.

Increased Input Resistance in Human Dendrites

To directly assess the properties of human apical dendrites, we performed dendritic whole-cell recordings up to 1,834 µm from the soma (Figure 2). Rodent L5 apical dendrites are known to possess high densities of ion channels, including hyperpolarization-activated cyclic nucleotide-gated (HCN) channels (Atkinson and Williams, 2009; Harnett et al., 2015; Kole et al., 2006; Williams and Stuart, 2000), resulting in low input resistance and prominent voltage sag. Using local hyperpolarizing current injections, we mapped the subthreshold properties of rat and human dendrites at various distances from the soma (Figures 2A and 2B; rat: n = 88 recordings from 22 rats; human: n = 42 recordings from 7 patients). We observed an increase in voltage sag as a function of distance in both groups (Figure 2C), but the distance-dependent profile in human neurons extended across their greater length. Interestingly, input resistance was dramatically larger in human distal dendrites (Figures 2C and S1; median [Q1–Q3]: 15.7 [13.7–19.5] versus 35.1 [29.8–47.9] MΩ, ***$p < 10^{-12}$, Wilcoxon rank sum test; rat: n = 72 recordings from 19 rats; human: n = 26 recordings from 7 patients). Despite the apparent enrichment of HCN channels in distal human dendrites, higher resistance indicates that human dendrites may possess fewer open conductances at rest.

We ensured that dendritic properties were not affected by methodological issues associated with the acquisition of human tissue. We used the same slicing procedure in terms of equipment, solutions, recovery time, and slice thickness for human and rat brains. Because of the transport of human tissue from the hospital, the time from brain extraction to slicing differed for the two groups. However, we found no differences in dendritic excitability between rat slices that were directly sliced and those that underwent a sham transport (25 min in the same cooler used to transport human samples; Figure S3). We also controlled for the impact of cut dendritic branches during slicing and the incubation time after slicing (Figure S3). Finally, we used adult rats and human tissue from adult patients to avoid age-dependent changes (Atkinson and Williams, 2009) in dendritic properties (Figure S3).

Enhanced Electrical Compartmentalization in Human Neurons

We next measured signal transfer with multi-site dendritic or somato-dendritic recordings (Figures 3A–3D). For a similar

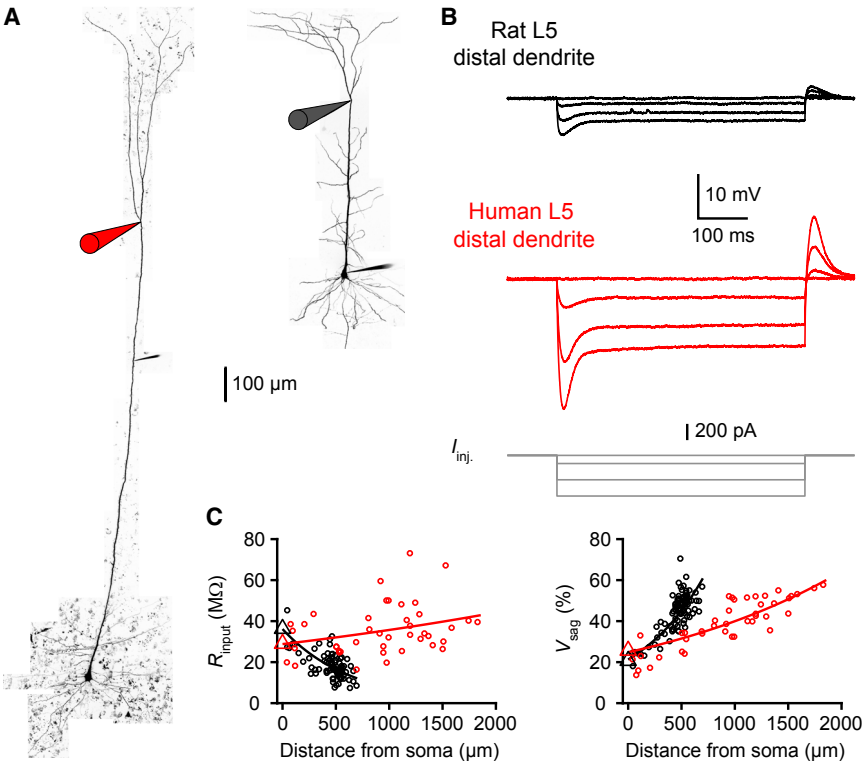

Figure 2. Increased Input Resistance in Human Dendrites

(A) Two-photon z stack montage image of human (left) and rat (right) L5 neurons with distal patch-clamp electrodes (1,374 and 531 µm from the soma, respectively).

(B) Rat (top) and human (middle) dendritic voltage in response to step current injections (bottom) from the neurons in (A).

(C) Input resistance (left) and voltage sag (right) as a function of distance from the soma (rat: n = 88 recordings from 22 rats; human: n = 42 recordings from 7 patients). Triangles are somatic averages and lines are exponential fit to the data.

See also Figures S1 and S3.

distance, voltage spread toward the soma was conserved in rat and human dendrites (Figure 3E and 3G). The half attenuation points (Figure 3E) were not statistically different (50% attenuation [95% CI]: 453 [406, 531] versus 456 [384, 536] µm; rat: n = 17 recordings from 9 rats; human: n = 16 recordings from 4 patients). However, because human dendrites were much longer, the attenuation experienced by distal dendrites was much more pronounced (Figure 3G). Voltage transfer is dependent on the impedance profile of the neurons and will be lower for transfer from high to low impedance compartments. Because rat distal dendrites had much lower impedance than rat soma, backward attenuation was stronger than forward attenuation (Figure 3E). The impedance profile of human neurons diverged significantly, such that backward attenuation (Figure 3F) was less severe than forward attenuation (50% attenuation [95% CI]: 277 [248, 305] versus 533 [467, 582] µm; rat: n = 19 recordings from 10 rats; human: n = 15 recordings from 3 patients). Overall, distal dendrites were more electrically remote from the soma in human neurons, and the attenuation of distal inputs toward the soma was especially strong. Thus, the longer physical length of human neurons translates into a longer electrotonic length.

Capacitive filtering contributes to dendritic compartmentalization, but its influence on steady-state voltage attenuation is rather limited. Specific membrane capacitance has recently been suggested to be ~0.5 µF/cm^2 in human neurons as opposed to ~1.0 µF/cm^2 in rodent neurons (Eyal et al., 2016). Lower capacitance was predicted to limit the attenuation of transient events, such as excitatory postsynaptic potentials (EPSPs). We directly tested the spread of phasic signals by injecting EPSC-shaped currents in multi-site recordings (Figure S4). We found that EPSP attenuation toward the soma was similar in rat and human neurons (50% attenuation [95% CI]: 408 [328, 470] versus 417 [350, 485] µm; rat: n = 13 recordings from 8 rats; human: n = 11 recordings from 2 patients), with backward attenuation being slightly less pronounced in human neurons (50% attenuation [95% CI]: 474 [442, 513] versus 683 [570, 880] µm; rat: n = 14 recordings from 9 rats; human: n = 10 recordings from 2 patients). These results are consistent with our findings for steady-state attenuation and demonstrate that the spread of EPSPs is not facilitated in human L5 neurons. Moreover, somatic and dendritic impedance profile in response to current sinewaves of increasing frequencies were similar across species, and dendritic effective time constants were larger in human neurons (Figure S1). Thus, the integrative properties of human neurons are inconsistent with lower capacitive filtering. However, other factors, such as HCN channels (Vaidya and Johnston, 2013), influence these functional properties. We therefore directly measured specific membrane capacitance in nucleated patches. We found that rat and human L5 neurons both had specific membrane capacitance values ~0.9 (Figure S4), consistent with previous rodent L5 measurements (Gentet et al., 2000). Together with functional evidence, our nucleated patch recordings establish that capacitance is not lower in human L5 neurons. Our results demonstrate that both resistive and capacitive filtering are more pronounced in human neurons due to their increased length and suggest the absence of compensatory mechanisms.

Compartmentalization Limits Dendritic Spikes and Somatic Bursts in Human Neurons

Distal inputs can be amplified by voltage-gated ion channels to overcome electrical compartmentalization: therefore, we compared the active properties of human and rat dendrites. In a rat neuron, current injection near the main bifurcation point (536 µm from the soma) triggered typical wide dendritic spikes coupled to somatic bursts (Figure 4B) (Harnett et al., 2013; Larkum and Zhu, 2002; Larkum et al., 2001; Major et al., 2013;

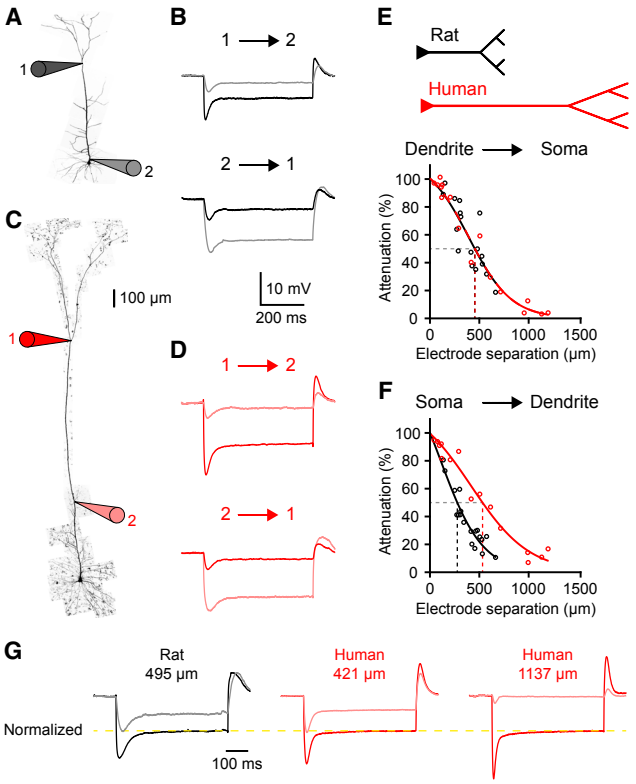

Figure 3. Increased Electrical Compartmentalization in Human Neurons

(A) Two-photon image of a rat L5 neuron patched at the soma (2) and 579 µm away (1).

(B) Dendritic (1; black) and somatic (2; gray) voltage in response to dendritic (top) and somatic (bottom) step current injection of −500 pA.

(C) Two-photon image of a human L5 neuron patched 511 (2) and 1507 (1) µm from the soma (996 µm separation).

(D) Distal (1; red) and proximal (2; light red) dendritic voltage in response to distal (top) and proximal (bottom) step current injection of −500 pA.

(E) Distance-dependent steady-state attenuation toward the soma (rat: n = 17 recordings from 9 rats; human: n = 16 recordings from 4 patients). Lines represent logistic fit to the data. Dashed lines represent 50% attenuation.

(F) Distance-dependent steady-state attenuation toward the distal dendrites (rat: n = 19 recordings from 10 rats; human: n = 15 recordings from 3 patients).

(G) Distal and proximal voltage normalized to distal steady-state voltage (yellow line). For a comparable distance, rat (left) and human (middle) dendrites show similar attenuation. Due to their increased length, human dendrites experience more attenuation (right).

See also Figure S4.

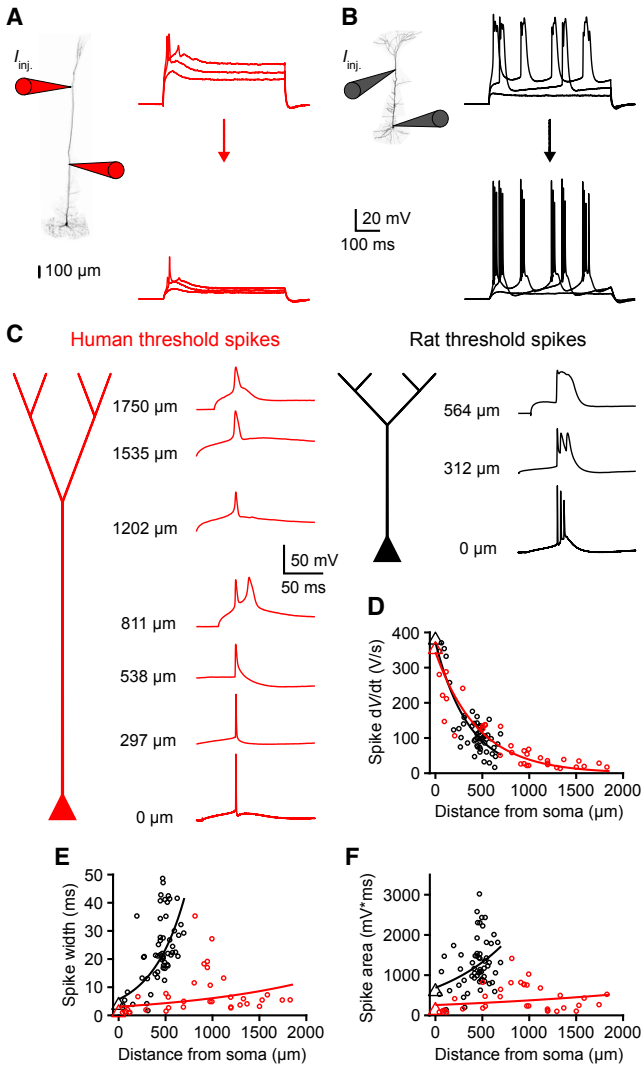

Figure 4. Weak Dendritic Spikes in Human Neurons

(A) Left: two-photon image of a human L5 neuron patched 535 and 1,256 µm from the soma. Right: distal (top) and proximal (bottom) dendritic voltage in response to distal current injection at rheobase and rheobase ± 100 pA.

(B) Left: two-photon image of a rat L5 neuron patched at the soma and 536 µm away. Right: distal dendritic (top) and somatic (bottom) voltage in response to dendritic current injection at rheobase and rheobase ± 100 pA.

(C) Example human (red) and rat (black) threshold spikes recorded in separate experiments. Spikes (backpropagating APs or locally initiated dendritic events) elicited with local rheobase current injections are shown at the indicated distances from the soma.

(D–F) Threshold spike properties as a function of distance from the soma (rat: n = 57 recordings from 21 rats; human: n = 34 recordings from 7 patients). Triangles are somatic medians and lines are exponential fit to the data. (D) Maximum spike d*V*/dt. (E) Spike width. (F) Spike area.

Williams, 2004; Williams and Stuart, 1999). However, current injection at a comparable site in a human neuron (1,256 µm from the soma) elicited dendritic spikes that failed on their way to the soma (Figure 4A). Furthermore, dendritic spikes were weaker in human dendrites with significantly reduced width and area (Figures 4E and 4F). The maximal instantaneous voltage change (d*V*/dt) decreased similarly with distance from the soma in rat and human neurons, such that distal human spikes had slower onsets (Figure 4D). Together, these features indicate that distal dendritic integration has limited influence on somatic output in human neurons.

What underlies the distinct somatic and dendritic spike properties in human neurons? The properties and distributions of voltage-gated conductances controlling the initiation and propagation of spikes could be different. Alternatively, we reasoned that enhanced electrical segregation between somatic and dendritic compartments in human neurons might limit regenerative

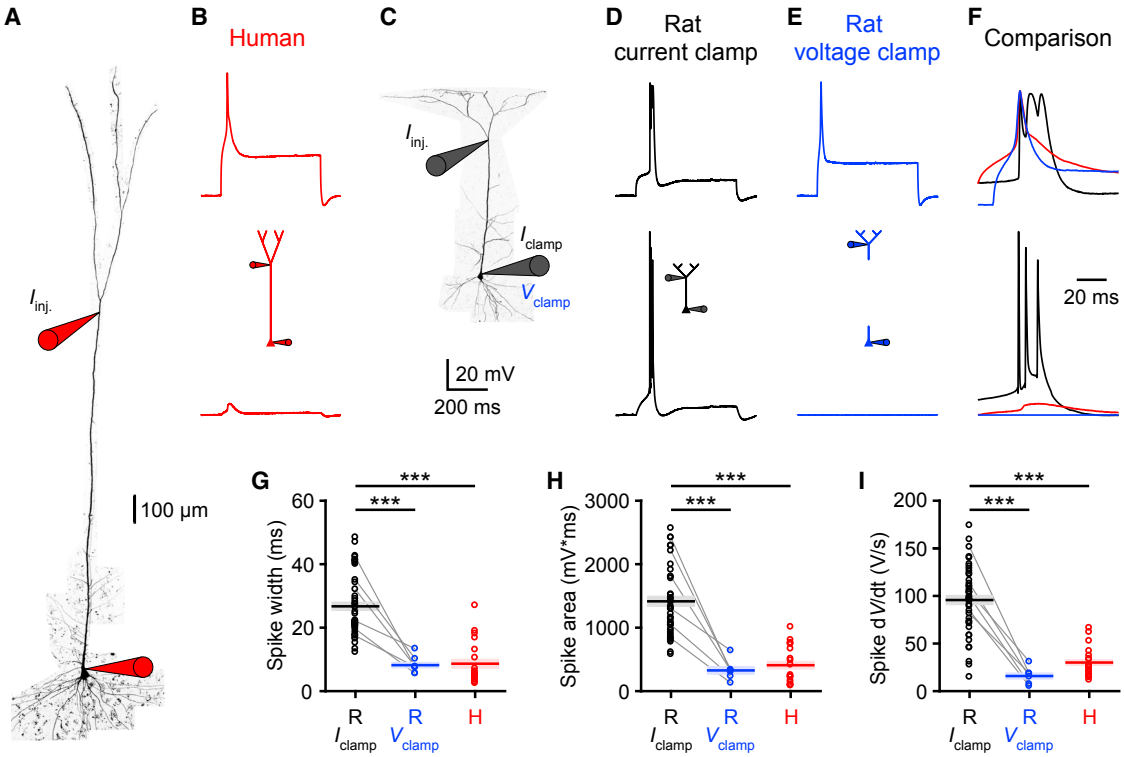

Figure 5. Increased Compartmentalization Limits Human Dendritic Spikes

(A) Two-photon image of a human L5 neuron patched at the soma and 982 µm away.

(B) Threshold dendritic spike (top) fails to elicit somatic AP (bottom) in the human neuron shown in (A).

(C) Two-photon image of a rat L5 neuron patched at the soma and 469 µm away.

(D) Under control conditions, the threshold dendritic spike (top) is associated with a somatic burst (bottom) in the rat neuron shown in (C).

(E) Under somatic voltage clamp to prevent APs (bottom), the threshold dendritic spike is weaker (top) in the rat neuron shown in (C).

(F) Comparison of dendritic and somatic voltage waveforms from (B)–(E).

(G–I) Properties of threshold spikes in distal (>400 µm and >900 µm from the soma in rats and humans, respectively) dendrites (rat: n = 43 recordings from 17 rats; human: n = 19 recordings from 4 patients). Gray lines link paired measurements for rat dendrites under current clamp and voltage clamp (n = 6 recordings from 5 rats). Pooled data represent mean ± SEM. One-way ANOVA followed by multiple comparison tests were used for statistical comparison (***$p < 10^{-10}$ ANOVA, ***$p < 10^{-5}$ R-I_{Clamp} versus R-V_{Clamp}, ***$p < 10^{-4}$ R-I_{Clamp} versus H, $p > 0.5$ R-V_{Clamp} versus H). (G) Spike width. (H) Spike area. (I) Maximum spike dV/dt. See also Figure S5.

interactions between the different compartments. To test these scenarios, we designed a novel approach to dissociate dendritic spikes from somatic APs in rat neurons, mimicking the increased compartmentalization of human neurons (Figure 5). We predicted that decoupling rat neurons would result in human-like spike properties if voltage-gated conductances are conserved. First, we used somatic voltage clamp to silence the soma (Figures 5E and S5). This manipulation did not prevent dendritic depolarization due to poor space-clamp (Beaulieu-Laroche and Harnett, 2018; Dembrow and Zemelman, 2015; Spruston et al., 1993; Tran-Van-Minh et al., 2016; Williams and Mitchell, 2008). By preventing somatic AP generation, we observed much narrower dendritic spikes in response to dendritic current injection (Figures 5E and 5F). Somatic voltage clamp effectively converted rat distal dendritic spikes into human dendritic spikes in terms of width, area, and dV/dt (Figures 5G–5I). Next, we performed the converse experiment to test whether somatic AP bursts were dependent on active interactions with distal dendrites. We voltage clamped rat mid-distal (378 ± 39 µm from the soma, n = 8 recordings from 5 rats) dendrites during somatic current injections to prevent dendritic electrogenesis (Figures 6A–6C and S6). APs were still elicited, but artificially decoupling the dendrites completely eliminated burst firing (Figures 6F and 6G). Thus, our voltage-clamp experiments indicate that the distinct human spike properties represent weaker somato-dendritic coupling rather than different complements of voltage-gated ion channels.

Stretched Ion Channel Distributions in Human Neurons

How do ionic conductances compare in rat and human dendrites? Our voltage-clamp experiments and the similar voltage sag indicate that rat and human dendrites possess similar ion channel distributions. However, the size difference between the two neuron types suggests a redistribution of the conductances. We constructed a biophysical rat L5 pyramidal neuron model constrained by our recordings (Figures 7A–7C; STAR Methods) and evaluated two alternative mechanisms to extend the model to the length of a human neuron: stretching and

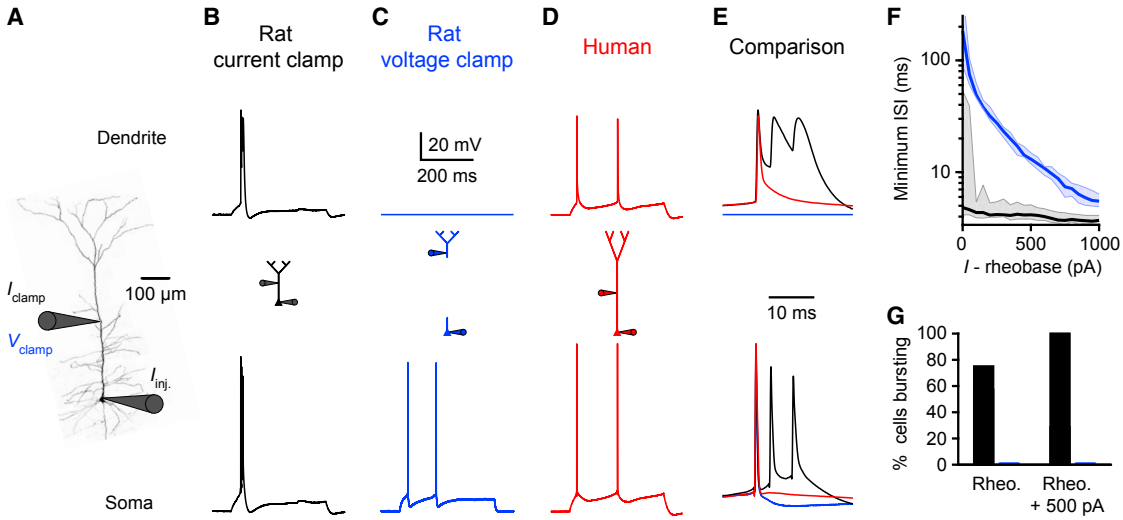

Figure 6. Increased Compartmentalization Limits Somatic Burst Firing in Human Neurons

(A) Two-photon image of a rat L5 neuron patched at the soma and 312 µm away.

(B) Somatic APs (bottom) and dendritic spike (top) in response to somatic current injection in a rat neuron. Under control conditions, somatic current injection elicits high-frequency AP bursts associated with dendritic spikes.

(C) Under dendritic voltage clamp (top), somatic current injection elicits low-frequency APs (bottom).

(D) Somatic (bottom) and dendritic (top; 510 µm from the soma) voltage in response to somatic current injection in a human neuron.

(E) Comparison of dendritic (top) and somatic (bottom) voltage waveforms from (B)–(D).

(F) Minimum ISI as a function of injected current above rheobase (n = 8 recordings from 5 rats). Population medians with 95% confidence intervals are shown.

(G) Percentage of neurons exhibiting bursts (>150 Hz) at rheobase and rheobase + 500 pA.

See also Figure S6.

scaling. Stretching the apical dendrites without affecting the relative distribution and total numbers of ion channels (Figure 7B) reproduced the reduced somato-dendritic coupling and the distinct human spike properties (Figure 7D). Surprisingly, a scaled model, where local ion channel densities were maintained such that total numbers of channels increased, failed to capture the limited coupling of human neurons (Figure S7). Our simulations therefore suggest that both ionic channel densities and gradients are stretched in human dendrites, which could account for the higher input resistance we observed (Figure 2C).

We tested the model prediction that local ion channel densities are lower in human dendrites by directly measuring dendritic conductances. Following whole-cell recordings from distal dendrites, we pulled outside-out patches (Figures 7F–7H) of consistent sizes (pipette resistance: 10.44 ± 0.16 versus 10.44 ± 0.18 MΩ, p = 0.99, unpaired t test; rat: n = 56 recordings from 8 rats; human: n = 34 recordings from 2 patients). We recorded ensemble HCN-mediated currents with hyperpolarization steps (Harnett et al., 2015) and discovered that HCN ensemble currents were significantly smaller in human dendrites (Figures 7I and 7J; median [Q1–Q3]: 13.1 [8.9–21.3] versus 4.6 [3.3–8.0] pA, ***$p < 10^{-9}$, Wilcoxon rank sum test). In the same population of dendrites, input resistance was significantly higher in human dendrites (median [Q1–Q3]: 15.0 [13.5–17.7] versus 31.0 [29.8–43.0] MΩ, ***$p < 10^{-14}$, Wilcoxon rank sum test), consistent with Figures 2C and S1. These results suggest that lower ion channel densities underlie the increased input resistance of human dendrites, providing strong support for the stretched conductances model (Figure 7A).

DISCUSSION

Our understanding of synaptic integration stems almost exclusively from rodent studies. Here, we reveal that human cortical neurons exhibit distinct integrative properties. We find that the size of human neurons results in increased electrical compartmentalization, which changes their input-output properties. By artificially increasing compartmentalization in rat neurons, we demonstrate that enhanced compartmentalization underlies the weaker dendritic spikes and reduced somatic bursting of human neurons. Furthermore, we reveal that ion channel densities are decreased in human dendrites, suggesting that ionic conductances are more dispersed in the longer dendrites of human neurons. Compensatory mechanisms were not apparent. Contrary to a recent report (Eyal et al., 2016), we did not find lower specific membrane capacitance in human neurons (Figure S4). While rat L5 neurons may be comparable to human L2/3 neurons in terms of size, their electrophysiological properties (input resistance, voltage sag, and AP properties; Figures 1, S1, and S2) are more closely related to human L5 neurons. Our voltage-clamp experiments and stretched conductances model further support the notion that cell-type-dependent features are roughly conserved across species, consistent with the laminar expression patterns of most cell-type-specific genes being preserved (Zeng et al., 2012). Thus, human L5 neurons are approximately stretched rat L5 neurons that, due to elongation without compensatory changes, have unique integrative capabilities.

An important caveat in our study is the distinct origins of the rodent and human brain tissues. We standardized our slicing

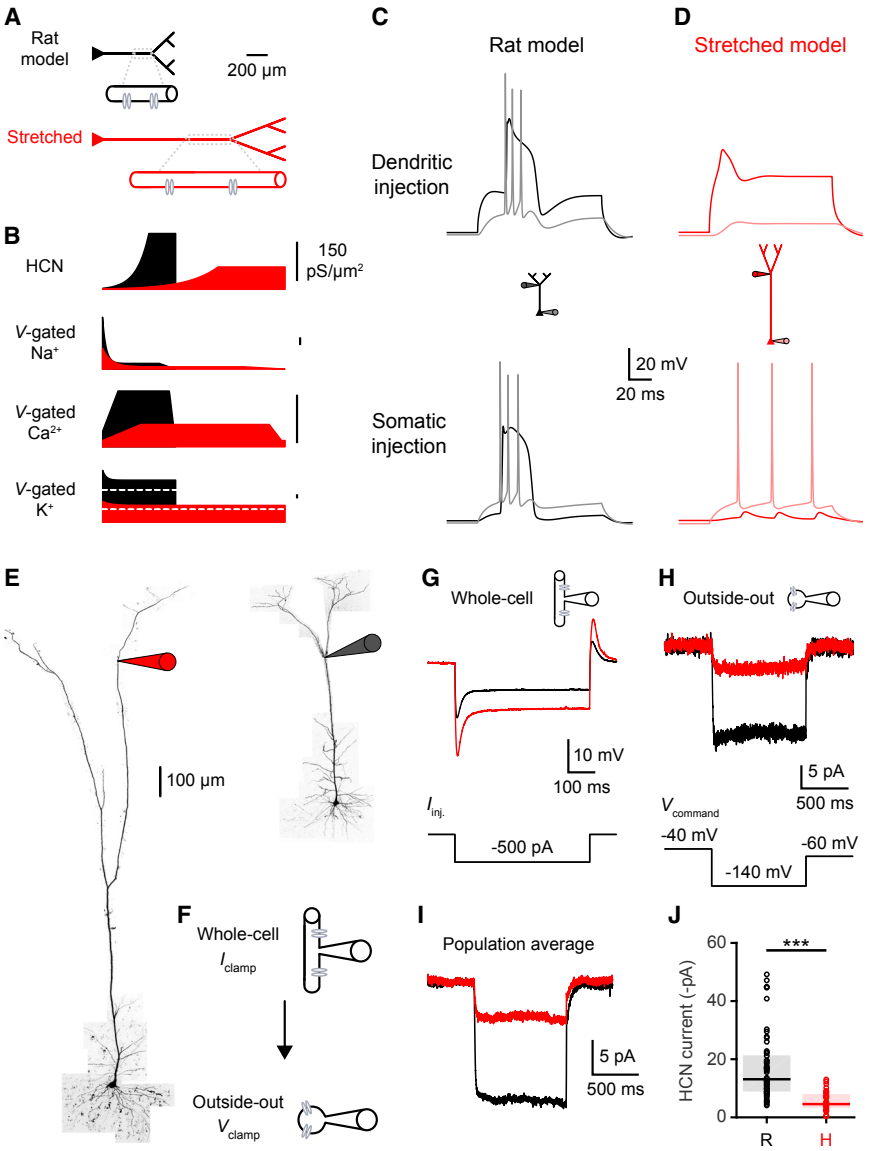

Figure 7. Stretched Ion Channel Distributions in Human Neurons

(A) Biophysical model. Top: rat model with schematic density of ion channels in a dendritic segment. Bottom: stretched model where the apical dendrites are lengthened without affecting the total number of ion channels. See also Table S2 and Figure S7.

(B) Distance-dependent rat (black) and stretched (red) distribution of voltage-gated ion channels. Transient and persistent voltage-gated potassium channel distributions are illustrated below and above the white dashed lines, respectively.

(C) Rat model with dendritic voltage in black and somatic voltage in gray. Top: the threshold dendritic spike is associated with a somatic burst. Bottom: high-frequency APs are coupled to a dendritic spike.

(D) Stretched model with dendritic voltage in red and somatic voltage in light red. Top: the threshold dendritic spike fails to elicit somatic AP. Bottom: low-frequency somatic APs fail to engage distal dendrites.

(E) Two-photon z stack montage image of human (left) and rat (right) L5 neurons with distal patch-clamp electrodes (1,514 and 514 µm from the soma, respectively).

(F) Whole-cell recordings were used to measure subthreshold properties, including input resistance and voltage sag. Outside-out patches were subsequently pulled from the same location to measure the local density of HCN channels.

(G) Whole-cell voltage waveforms in the rat (black) and human (red) dendrites illustrated in (E) in response to a hyperpolarizing current step (bottom).

(H) Top: ensemble HCN currents recorded in outside-out patches excised from the rat (black) and human (red) dendrites illustrated in (E). Bottom: voltage-clamp protocol.

(I and J) Ensemble HCN current properties in distal (>400 µm and >900 µm from the soma in rats and humans, respectively; ranging 55%–85% of the distance from the soma to the pia) dendrites (rat: n = 56 recordings from 8 rats; human: n = 34 recordings from 2 patients). (I) Population average of ensemble HCN currents. (J) HCN steady-state currents (***$p < 10^{-9}$, Wilcoxon rank sum test). Pooled data represent median and interquartile range.

approach across species and controlled for numerous factors, including age, transport, and time after slicing (Figure S3). Nevertheless, the disease etiology, pharmacological treatment, and anesthesia procedure could influence dendritic integration. Our non-pathologic samples came from a population of epileptic patients, but previous studies with more extensive patient history and surgery types failed to observe significant correlations between disease history and dendritic morphology (Mohan et al., 2015) or synaptic plasticity (Verhoog et al., 2013). Despite no concrete evidence yet that disease and medical treatment affect the basic physiological properties of neocortical neurons, this continues to be an important concern for research involving human tissue.

Humans have the thickest cortex among mammals (except for manatees) (Defelipe, 2011; DeFelipe et al., 2002; Mota and Herculano-Houzel, 2015; Sun and Hevner, 2014), indicating that human neurons possess exceptionally long and compartmentalized apical dendrites. In rodent neurons, distal inputs arriving in supragranular layers can drive repetitive somatic spikes with the help of dendritic spikes (Figure 4B). The increased electrotonic length of human dendrites disrupts this relationship; distal inputs provide very little excitation to the soma even with dendritic spikes. This arrangement may seem counterintuitive: distal synaptic integration would incur significant metabolic costs without purpose. However, this extreme electrical isolation may be evolutionarily advantageous from a computational standpoint. Theoretical studies have proposed that dendritic compartments can perform parallel processing as well as subsequent nonlinear transformations prior to final integration at the axon (Häusser and Mel, 2003; Jadi et al.,

2014; London and Häusser, 2005; Poirazi et al., 2003; Polsky et al., 2004; Tran-Van-Minh et al., 2015). Recent experimental evidence in rodents also supports the role of dendritic processing in cortical computation (Cichon and Gan, 2015; Harnett et al., 2013; Lavzin et al., 2012; Schmidt-Hieber et al., 2017; Smith et al., 2013; Takahashi et al., 2016; Xu et al., 2012). With more isolated or additional compartments capable of nonlinear transformations, the electrical structure of human dendrites could provide single neurons with a richer computational repertoire. However, other factors not studied here, such as the patterns of synaptic inputs and neuromodulatory control, may compensate *in vivo* for the increased length of human neurons. Is extreme compartmentalization in human dendrites a bug (Häusser and Mel, 2003) necessitating correction or a feature that enhances computational power? We demonstrate here that the integrative properties of human and rat neurons differ *ex vivo*, but future work is needed to determine how these intrinsic features interact with circuit factors *in vivo* to mediate cortical computation.

STAR★METHODS

Detailed methods are provided in the online version of this paper and include the following:

- KEY RESOURCES TABLE
- CONTACT FOR REAGENT AND RESOURCE SHARING
- EXPERIMENTAL MODEL AND SUBJECT DETAILS
- METHOD DETAILS
  - Human slice preparation
  - Rat slice preparation
  - Patch-clamp recording
  - Compartmental modeling
- QUANTIFICATION AND STATISTICAL ANALYSIS

SUPPLEMENTAL INFORMATION

Supplemental Information includes seven figures and two tables and can be found with this article online at https://doi.org/10.1016/j.cell.2018.08.045.

A video abstract is available at https://doi.org/10.1016/j.cell.2018.08.045#mmc2.

ACKNOWLEDGMENTS

We thank Robert Desimone, Michale Fee, Sabbi Lall, and Michael Tadross for comments on the manuscript, as well as Richard Naud and Aaron Milstein for constructive criticism on the modeling. We also thank Jakob Voigts for help with statistical analyses and Yangling Chou for assistance in acquiring human tissue. We acknowledge the support of the Natural Sciences and Engineering Research Council of Canada (NSERC) (PGSD2-517068-2018 to L.B.-L.), the Dana Foundation David Mahoney Neuroimaging Grant Program, the NIH (RO1NS106031), and the Klingenstein-Simons Fellowship Awards in Neuroscience (M.T.H.).

AUTHOR CONTRIBUTIONS

L.B.-L. designed the experiments, prepared slices, performed dendritic and somatic recordings, analyzed the data, contributed to biophysical modeling, prepared the figures, and wrote the manuscript. E.H.S.T. performed biophysical modeling, created analysis tools, and contributed to slicing. M.-S.v.d.G. contributed to slicing and somatic recordings. M.L. contributed to somatic recordings. D.B. contributed to tissue transport and slicing. Z.M.W. and E.N.E. performed the surgeries that resulted in the human tissue. M.P.F. oversaw removal and parcellation of that tissue, as well as overall IRB and human subject regulatory aspects of the project. S.S.C. helped in designing methods for acquiring human tissue and ensured that the tissue was collected. He also participated in the design and interpretation of the experiments. M.T.H. conceived of and supervised the project.

DECLARATION OF INTERESTS

The authors declare no competing interests.

Received: February 12, 2018
Revised: June 11, 2018
Accepted: August 17, 2018
Published: October 18, 2018

REFERENCES

Atkinson, S.E., and Williams, S.R. (2009). Postnatal development of dendritic synaptic integration in rat neocortical pyramidal neurons. J. Neurophysiol. *102*, 735–751.

Beaulieu-Laroche, L., and Harnett, M.T. (2018). Dendritic spines prevent synaptic voltage clamp. Neuron *97*, 75–82.

Carnevale, N.T., and Hines, M.L. (2006). The Neuron Book (Cambridge: Cambridge University Press).

Cichon, J., and Gan, W.B. (2015). Branch-specific dendritic Ca(2+) spikes cause persistent synaptic plasticity. Nature *520*, 180–185.

Connors, B.W., Gutnick, M.J., and Prince, D.A. (1982). Electrophysiological properties of neocortical neurons in vitro. J. Neurophysiol. *48*, 1302–1320.

de Kock, C.P., and Sakmann, B. (2008). High frequency action potential bursts (>or= 100 Hz) in L2/3 and L5B thick tufted neurons in anaesthetized and awake rat primary somatosensory cortex. J. Physiol. *586*, 3353–3364.

Defelipe, J. (2011). The evolution of the brain, the human nature of cortical circuits, and intellectual creativity. Front. Neuroanat. *5*, 29.

DeFelipe, J., Alonso-Nanclares, L., and Arellano, J.I. (2002). Microstructure of the neocortex: comparative aspects. J. Neurocytol. *31*, 299–316.

Dembrow, N.C., and Zemelman, B.V. (2015). Temporal dynamics of L5 dendrites in medial prefrontal cortex regulate integration versus coincidence detection of afferent inputs. J. Neurosci. *35*, 4501–4514.

Dembrow, N.C., Chitwood, R.A., and Johnston, D. (2010). Projection-specific neuromodulation of medial prefrontal cortex neurons. J. Neurosci. *30*, 16922–16937.

Elston, G.N., Benavides-Piccione, R., and DeFelipe, J. (2001). The pyramidal cell in cognition: a comparative study in human and monkey. J. Neurosci. *21*, RC163.

Eyal, G., Verhoog, M.B., Testa-Silva, G., Deitcher, Y., Lodder, J.C., Benavides-Piccione, R., Morales, J., DeFelipe, J., de Kock, C.P., Mansvelder, H.D., and Segev, I. (2016). Unique membrane properties and enhanced signal processing in human neocortical neurons. Elife *5*, e16553.

Gentet, L.J., Stuart, G.J., and Clements, J.D. (2000). Direct measurement of specific membrane capacitance in neurons. Biophys. J. *79*, 314–320.

Guerguiev, J., Lillicrap, T.P., and Richards, B.A. (2017). Towards deep learning with segregated dendrites. Elife *6*, e22901.

Halgren, M., Fabó, D., Ulbert, I., Madsen, J.R., Erőss, L., Doyle, W.K., Devinsky, O., Schomer, D., Cash, S.S., and Halgren, E. (2018). Superficial slow rhythms integrate cortical processing in humans. Sci. Rep. *8*, 2055.

Harnett, M.T., Makara, J.K., Spruston, N., Kath, W.L., and Magee, J.C. (2012). Synaptic amplification by dendritic spines enhances input cooperativity. Nature *491*, 599–602.

Harnett, M.T., Xu, N.L., Magee, J.C., and Williams, S.R. (2013). Potassium channels control the interaction between active dendritic integration compartments in layer 5 cortical pyramidal neurons. Neuron *79*, 516–529.

Harnett, M.T., Magee, J.C., and Williams, S.R. (2015). Distribution and function of HCN channels in the apical dendritic tuft of neocortical pyramidal neurons. J. Neurosci. *35*, 1024–1037.

Hattox, A.M., and Nelson, S.B. (2007). Layer V neurons in mouse cortex projecting to different targets have distinct physiological properties. J. Neurophysiol. *98*, 3330–3340.

Häusser, M., and Mel, B. (2003). Dendrites: bug or feature? Curr. Opin. Neurobiol. *13*, 372–383.

Hay, E., Hill, S., Schürmann, F., Markram, H., and Segev, I. (2011). Models of neocortical layer 5b pyramidal cells capturing a wide range of dendritic and perisomatic active properties. PLoS Comput. Biol. *7*, e1002107.

Jadi, M.P., Behabadi, B.F., Poleg-Polsky, A., Schiller, J., and Mel, B.W. (2014). An augmented two-layer model captures nonlinear analog spatial integration effects in pyramidal neuron dendrites. Proc. IEEE Inst. Electr. Electron Eng. *102*, 1.

Kim, E.J., Juavinett, A.L., Kyubwa, E.M., Jacobs, M.W., and Callaway, E.M. (2015). Three types of cortical layer 5 neurons that differ in brain-wide connectivity and function. Neuron *88*, 1253–1267.

Kole, M.H., Hallermann, S., and Stuart, G.J. (2006). Single Ih channels in pyramidal neuron dendrites: properties, distribution, and impact on action potential output. J. Neurosci. *26*, 1677–1687.

Larkum, M.E., and Zhu, J.J. (2002). Signaling of layer 1 and whisker-evoked Ca2+ and Na+ action potentials in distal and terminal dendrites of rat neocortical pyramidal neurons in vitro and in vivo. J. Neurosci. *22*, 6991–7005.

Larkum, M.E., Zhu, J.J., and Sakmann, B. (2001). Dendritic mechanisms underlying the coupling of the dendritic with the axonal action potential initiation zone of adult rat layer 5 pyramidal neurons. J. Physiol. *533*, 447–466.

Larkum, M.E., Nevian, T., Sandler, M., Polsky, A., and Schiller, J. (2009). Synaptic integration in tuft dendrites of layer 5 pyramidal neurons: a new unifying principle. Science *325*, 756–760.

Lavzin, M., Rapoport, S., Polsky, A., Garion, L., and Schiller, J. (2012). Nonlinear dendritic processing determines angular tuning of barrel cortex neurons in vivo. Nature *490*, 397–401.

London, M., and Häusser, M. (2005). Dendritic computation. Annu. Rev. Neurosci. *28*, 503–532.

Magee, J.C. (2000). Dendritic integration of excitatory synaptic input. Nat. Rev. Neurosci. *1*, 181–190.

Mainen, Z.F., and Sejnowski, T.J. (1996). Influence of dendritic structure on firing pattern in model neocortical neurons. Nature *382*, 363–366.

Major, G., Larkum, M.E., and Schiller, J. (2013). Active properties of neocortical pyramidal neuron dendrites. Annu. Rev. Neurosci. *36*, 1–24.

Mohan, H., Verhoog, M.B., Doreswamy, K.K., Eyal, G., Aardse, R., Lodder, B.N., Goriounova, N.A., Asamoah, B., B Brakspear, A.B., Groot, C., et al. (2015). Dendritic and axonal architecture of individual pyramidal neurons across layers of adult human neocortex. Cereb. Cortex *25*, 4839–4853.

Mota, B., and Herculano-Houzel, S. (2015). Brain structure. Cortical folding scales universally with surface area and thickness, not number of neurons. Science *349*, 74–77.

Petreanu, L., Mao, T., Sternson, S.M., and Svoboda, K. (2009). The subcellular organization of neocortical excitatory connections. Nature *457*, 1142–1145.

Poirazi, P., Brannon, T., and Mel, B.W. (2003). Pyramidal neuron as two-layer neural network. Neuron *37*, 989–999.

Polsky, A., Mel, B.W., and Schiller, J. (2004). Computational subunits in thin dendrites of pyramidal cells. Nat. Neurosci. *7*, 621–627.

Ramaswamy, S., and Markram, H. (2015). Anatomy and physiology of the thick-tufted layer 5 pyramidal neuron. Front. Cell. Neurosci. *9*, 233.

Schiller, J., Schiller, Y., Stuart, G., and Sakmann, B. (1997). Calcium action potentials restricted to distal apical dendrites of rat neocortical pyramidal neurons. J. Physiol. *505*, 605–616.

Schiller, J., Major, G., Koester, H.J., and Schiller, Y. (2000). NMDA spikes in basal dendrites of cortical pyramidal neurons. Nature *404*, 285–289.

Schmidt-Hieber, C., Toleikyte, G., Aitchison, L., Roth, A., Clark, B.A., Branco, T., and Hausser, M. (2017). Active dendritic integration as a mechanism for robust and precise grid cell firing. Nat. Neurosci. *20*, 1114–1121.

Shai, A.S., Anastassiou, C.A., Larkum, M.E., and Koch, C. (2015). Physiology of layer 5 pyramidal neurons in mouse primary visual cortex: coincidence detection through bursting. PLoS Comput. Biol. *11*, e1004090.

Smith, S.L., Smith, I.T., Branco, T., and Häusser, M. (2013). Dendritic spikes enhance stimulus selectivity in cortical neurons in vivo. Nature *503*, 115–120.

Spruston, N. (2008). Pyramidal neurons: dendritic structure and synaptic integration. Nat. Rev. Neurosci. *9*, 206–221.

Spruston, N., Jaffe, D.B., Williams, S.H., and Johnston, D. (1993). Voltage- and space-clamp errors associated with the measurement of electrotonically remote synaptic events. J. Neurophysiol. *70*, 781–802.

Stuart, G., and Spruston, N. (1998). Determinants of voltage attenuation in neocortical pyramidal neuron dendrites. J. Neurosci. *18*, 3501–3510.

Sun, T., and Hevner, R.F. (2014). Growth and folding of the mammalian cerebral cortex: from molecules to malformations. Nat. Rev. Neurosci. *15*, 217–232.

Takahashi, N., Oertner, T.G., Hegemann, P., and Larkum, M.E. (2016). Active cortical dendrites modulate perception. Science *354*, 1587–1590.

Tran-Van-Minh, A., Cazé, R.D., Abrahamsson, T., Cathala, L., Gutkin, B.S., and DiGregorio, D.A. (2015). Contribution of sublinear and supralinear dendritic integration to neuronal computations. Front. Cell. Neurosci. *9*, 67.

Tran-Van-Minh, A., Abrahamsson, T., Cathala, L., and DiGregorio, D.A. (2016). Differential dendritic integration of synaptic potentials and calcium in cerebellar interneurons. Neuron *91*, 837–850.

Vaidya, S.P., and Johnston, D. (2013). Temporal synchrony and gamma-to-theta power conversion in the dendrites of CA1 pyramidal neurons. Nat. Neurosci. *16*, 1812–1820.

Verhoog, M.B., Goriounova, N.A., Obermayer, J., Stroeder, J., Hjorth, J.J.J., Testa-Silva, G., Baayen, J.C., de Kock, C.P.J., Meredith, R.M., and Mansvelder, H.D. (2013). Mechanisms underlying the rules for associative plasticity at adult human neocortical synapses. J. Neurosci. *33*, 17197–17208.

Williams, S.R. (2004). Spatial compartmentalization and functional impact of conductance in pyramidal neurons. Nat. Neurosci. *7*, 961–967.

Williams, S.R., and Mitchell, S.J. (2008). Direct measurement of somatic voltage clamp errors in central neurons. Nat. Neurosci. *11*, 790–798.

Williams, S.R., and Stuart, G.J. (1999). Mechanisms and consequences of action potential burst firing in rat neocortical pyramidal neurons. J. Physiol. *521*, 467–482.

Williams, S.R., and Stuart, G.J. (2000). Site independence of EPSP time course is mediated by dendritic I(h) in neocortical pyramidal neurons. J. Neurophysiol. *83*, 3177–3182.

Williams, S.R., and Stuart, G.J. (2002). Dependence of EPSP efficacy on synapse location in neocortical pyramidal neurons. Science *295*, 1907–1910.

Xu, N.L., Harnett, M.T., Williams, S.R., Huber, D., O'Connor, D.H., Svoboda, K., and Magee, J.C. (2012). Nonlinear dendritic integration of sensory and motor input during an active sensing task. Nature *492*, 247–251.

Zeng, H., Shen, E.H., Hohmann, J.G., Oh, S.W., Bernard, A., Royall, J.J., Glattfelder, K.J., Sunkin, S.M., Morris, J.A., Guillozet-Bongaarts, A.L., et al. (2012). Large-scale cellular-resolution gene profiling in human neocortex reveals species-specific molecular signatures. Cell *149*, 483–496.

STAR★METHODS

KEY RESOURCES TABLE

REAGENT or RESOURCE	SOURCE	IDENTIFIER
Biological Samples		
Human resected temporal cortex	Department of Pathology, Massachusetts General Hospital, Boston MA, USA	N/A
Chemicals, Peptides, and Recombinant Proteins		
Adenosine 5′-triphosphate magnesium salt	Sigma	Cat#: A9187; CAS: 74804-12-9
Alexa Fluor 488 hydrazide	Invitrogen	Cat#: A10436
Alexa Fluor 594 hydrazide	Invitrogen	Cat#: A10438
Calcium chloride dihydrate	Sigma	Cat#: 223506; CAS: 10035-04-8
D-(+)-Glucose	Sigma	Cat#: G7021; CAS: 50-99-7
Guanosine 5′-triphosphate sodium salt hydrate	Sigma	Cat#: G8877; CAS: 36051-31-7
HEPES	Sigma	Cat#: H3375; CAS: 7365-45-9
Isoflurane	Patterson Veterinary	Cat#: 07-893-1389
Magnesium chloride hexahydrate	Sigma	Cat#: 63068; CAS: 7791-18-6
Oregon Green 488 BAPTA-1, Hexapotassium Salt, cell impermeant	Invitrogen	Cat#: O6806
Phosphocreatine di(tris) salt	Sigma	Cat#: P1937; CAS: 108321-17-1
Potassium chloride	Sigma	Cat#: 60128; CAS: 7447-40-7
Potassium D-gluconate	Sigma	Cat#: G4500; CAS: 299-27-4
(+)-Sodium L-ascorbate	Sigma	Cat#: 11140; CAS: 134-03-2
Sodium bicarbonate	Sigma	Cat#: 792519; CAS: 144-55-8
Sodium chloride	Sigma	Cat#: S7653; CAS: 7647-14-5
Sodium phosphate monobasic monohydrate	Sigma	Cat#: S9638; CAS: 10049-21-5
Sodium pyruvate	Sigma	Cat#: P2256; CAS: 113-24-6
Sucrose	Sigma	Cat#: S1888; CAS: 57-50-1
Tetrodotoxin citrate	Abcam	Cat#: ab120055; CAS: 18660-81-6
Tetrodotoxin	Tocris	Cat#: 1078; CAS: 4368-28-9
Experimental Models: Organisms/Strains		
Sprague Dawley rat	Charles River	Strain code: 400
Software and Algorithms		
ImageJ	National Institutes of Health	https://imagej.nih.gov/ij/index.html
MATLAB 9.1 (R2016b)	MathWorks	https://www.mathworks.com
Neuron 7.5	Carnevale and Hines, 2006	https://www.neuron.yale.edu/neuron/
Other		
Axopatch 200B	Axon Instruments	N/A
Dagan BVC-700A	Dagan corporation	N/A
Electro-optical modulator	Conoptics	M350-80
Leica VT1200 S Fully automated vibrating blade microtome	Leica	VT1200 S
Mai Tai DeepSee	Spectra-Physics	MAI TAI HP DS
Photosensor module	Hamamatsu	H7422A-40
Ultima *In Vitro* Multiphoton Microscope System	Bruker	N/A

CONTACT FOR REAGENT AND RESOURCE SHARING

Further information and requests for resources and reagents should be directed to and will be fulfilled by the Lead Contact, Mark T. Harnett (harnett@mit.edu).

EXPERIMENTAL MODEL AND SUBJECT DETAILS

Human tissue was obtained as discarded tissue from neurosurgical patients at the Massachusetts General Hospital in accordance with protocols approved by the Massachusetts General Hospital Internal Review Board (IRB). Consent was not required and sample size estimation was not employed because only discarded tissue was used. Patients were male or female adults aged 20-42 years. We report only the sex of the patients because information on their gender identity was not available. Additional patient information is included in Table S1 (see Figure S3 for analyses on the impact of sex and age on dendritic properties). Samples were not allocated to distinct experimental groups.

Sprague Dawley rats (obtained from Charles River) were used in accordance with NIH and the Massachusetts Institute of Technology Committee on Animal Care guidelines. Male rats were housed in pairs or singly and used for experimentation at 3-7 months of age. Animals were maintained on a 12-hour light/dark cycle, in a temperature- and humidity-controlled room with food and water *ad libitum*.

METHOD DETAILS

Human slice preparation

Resected human tissue was considered discarded tissue after being examined by neuropathologists whose main objective was to ensure there was adequate tissue for diagnostic purposes. The neocortical tissue was obtained from the lateral anterior temporal lobe (middle and inferior temporal gyri) in patients undergoing resection of the temporal lobe including mesial structures for medically-intractable epilepsy. The neocortical tissue displayed no known abnormalities at the level of MRI scans, gross inspection, and subsequent microscopic examination as part of the standard neuropathologic assessment of the tissue. Patients undergoing resective surgery were primarily maintained under general anesthesia with propofol and remifentanil or sufentanil. Some cases utilized inhaled anesthetics, such as isoflurane or sevoflurane. For induction of general anesthesia, paralytic agents including rocuronium or succinylcholine as well as fentanyl were typically used. Resection usually occurred within 90 minutes of the start of the procedure.

After resection, tissue was placed within ~180 s in ice-cold slicing artificial cerebrospinal fluid (aCSF) containing (in mM): sucrose 160, sodium bicarbonate 28, potassium chloride 2.5, sodium phosphate monobasic monohydrate 1.25, calcium chloride 1, magnesium chloride 7.5, glucose 7.25, HEPES 20, sodium pyruvate 3, and sodium ascorbate 3, 295-305 mOsm, saturated with 95% O_2 and 5% CO_2. Samples were transported in sealed conditions for 20-35 minutes before being transferred to freshly oxygenated solution. Pia and surface blood vessels that would obstruct slicing were removed with forceps and samples were cut in small pieces (~3 mm x 3 mm) perpendicular (< 5 degrees off) to the surface of the brain. Slicing was performed with a vibrating blade microtome in ice-cold slicing aCSF. 300 μm slices were incubated for ~30 minutes at 35.5°C in recovery aCSF containing (in mM): sodium chloride 92, sodium bicarbonate 28.5, potassium chloride 2.5, sodium phosphate monobasic monohydrate 1.2, calcium chloride 2, magnesium chloride 4, glucose 25, HEPES 20, sodium pyruvate 3, and sodium ascorbate 5, 300-310 mOsm, saturated with 95% O_2 and 5% CO_2, or recording aCSF containing (in mM): sodium chloride 120, potassium chloride 3, sodium bicarbonate 25, sodium phosphate monobasic monohydrate 1.25, calcium chloride 1.2, magnesium chloride 1.2, glucose 11, sodium pyruvate 3, and sodium ascorbate 1, 302-305 mOsm, saturated with 95% O_2 and 5% CO_2. Slices were then stored at ~20°C until use. Incubation solutions were replaced every ~8 hours and recordings were performed up to 34 hours after slicing.

Rat slice preparation

Male rats were deeply anesthetized with isoflurane prior to immediate decapitation. 300 μm slices were prepared from temporal association cortex (TEA) (Eyal et al., 2016; Mohan et al., 2015). To obtain slices perpendicular to the surface of the brain, we performed a blocking cut in the frontal cortex of both hemispheres with a ~35° yaw angle off the coronal axis. The two hemispheres were glued on their frontal surface. The pia was completely removed from the cortical surface with fine forceps. Slicing and recovery were performed as described above for human slices. For experiments in Figures S3A–S3C, one brain hemisphere was placed in slicing aCSF in sealed conditions for 25 minutes before slicing. For initial pilot experiments, we employed usual rat methods (Beaulieu-Laroche and Harnett, 2018) where animals were deeply anesthetized with isoflurane prior to immediate decapitation or cardiac perfusion with rat slicing aCSF containing (in mM): sucrose 90, sodium chloride 60, sodium bicarbonate 26.5, potassium chloride 2.75, sodium phosphate monobasic monohydrate 1.25, calcium chloride 1.1, magnesium chloride 5, glucose 9, sodium pyruvate 3, and sodium ascorbate 1, 302-305 mOsm, saturated with 95% O_2 and 5% CO_2. Recordings were performed up to 13 hours after slicing.

Patch-clamp recording

Patch-clamp recordings were performed from the soma and apical dendrites of pyramidal neurons at 34–36°C in recording aCSF. Whole-cell current-clamp recordings were performed in bridge mode with an Axopatch 200B or a Dagan BVC-700A amplifier with bridge fully balanced. Whole-cell voltage-clamp recordings were performed with an Axopatch 200B amplifier with series resistance and whole-cell capacitance predicted and compensated > 80% and lag < 20 μs. Prediction and compensation were not set to their maximum as previously described (Beaulieu-Laroche and Harnett, 2018) to avoid ringing (large currents caused by dendritic spikes or backpropagating APs caused the voltage-clamp circuitry to oscillate). Two dendritic voltage-clamp recordings in Figure 6 were performed with the Dagan BVC-700A amplifier with series resistance compensated, which was similarly effective at preventing somatic burst firing. Patch pipettes from thick-wall glass (1.5 O.D., 0.75 I.D.) were used for voltage-clamp recordings to reduce capacitance. Current-clamp patch pipettes were prepared with thick-wall or thin-wall glass (1.5 O.D., 1.1 I.D.). Pipettes had resistances ranging from 3 to 15 MΩ, and capacitance was fully neutralized prior to break in. Series resistances ranged from 5-20 MΩ for soma and 8-30 MΩ for dendrites. Two closely spaced electrodes were used for some experiments to segregate current injection from voltage measurement (Beaulieu-Laroche and Harnett, 2018; Harnett et al., 2012; Williams, 2004; Williams and Mitchell, 2008). The intracellular solution contained (in mM): potassium gluconate 134, potassium chloride 6, HEPES 10, sodium chloride 4, adenosine 5′-triphosphate magnesium 4, guanosine 5′-triphosphate sodium 3, phosphocreatine di (tris) 14. Depending on the experiment, 0.05 Alexa 594, 0.1 Alexa 488, and/or 0.1 Oregon Green 488 BAPTA-1 were added to the intracellular solution. Liquid junction potential was not corrected for. Current and voltage signals were filtered at 10 kHz and acquired at 20 kHz.

Nucleated patches were obtained with thick-wall somatic patch pipettes (4-9 MΩ). Pipette capacitance was carefully compensated in cell-attached mode. 500-2000 steps of −5 mV from −60 mV were filtered at 100 kHz and acquired at 200 kHz with an Axopatch 200B amplifier. This protocol was run in cell-attached mode to capture small residual capacitive transients. The nucleated patch was pulled and the protocol was repeated 50 μm above the neuron (slightly above the slice) to minimize the changes in pipette capacitance. The residual cell-attached transient was subtracted from the nucleated patch transient.

Outside-out recordings with ∼10 MΩ thick-wall pipettes were performed with an Axopatch 200B amplifier. Following whole-cell characterization, the pipette was slowly withdrawn and the formation of an outside-out patch was confirmed under two-photon imaging (lack of cytoplasmic bridge). To record HCN channels, the voltage was stepped to −140 mV for 1000 ms followed by −60 mV for 1000 ms from a rest potential of −40 mV (Harnett et al., 2015). The protocol was repeated 3-18 times interleaved with 4 1/10 scaled protocol for leak subtraction. Current signals were filtered at 10 kHz and acquired at 20 kHz.

For all experiments except Figure S2, we recorded from large L5 pyramids with thick apical dendrites reaching L1 (Ramaswamy and Markram, 2015). As in previous rodent research, blind dendritic recordings were strongly biased toward thick apical dendrites that reliably originate from large L5 somas. In both rats and humans, we targeted the thickest dendrites and biggest L5 somas to isolate putative L5B neurons (Harnett et al., 2013, 2015; Hattox and Nelson, 2007; Hay et al., 2011). The anatomy and physiology of L5 neurons can vary across brain regions (Dembrow et al., 2010; Kim et al., 2015; Ramaswamy and Markram, 2015). To our knowledge, the present recordings are the first electrophysiological characterization of rat TEA L5 neurons, which are slightly more compact than rat L5 neurons in the primary somatosensory cortex, where most cortical dendritic physiology has been performed (Harnett et al., 2013, 2015; Larkum et al., 2001, 2009; Ramaswamy and Markram, 2015; Schiller et al., 1997; Shai et al., 2015; Williams, 2004; Williams and Stuart, 1999). In accordance with previous work (DeFelipe et al., 2002; Mohan et al., 2015) (http://help.brain-map.org/display/celltypes/Documentation), which places the beginning of L5 at ∼1.5 mm below the pia, we recorded human L5 neurons 1.5-2.2 mm below the pia. Rat L5 somas were located 650-950 μm below the pia. For L2/3 neurons (Figure S2), we targeted pyramidal neurons < 450 μm (rat) and < 1000 μm (human) from the pia.

A multiphoton microscope system with a Mai-Tai DeepSee laser was used to image Alexa 594 at 880 nm or Alexa 488 at 920 nm (separated via dichroic mirrors to independent sets of GaAsP photosensor modules). Another photosensor module was used to collect transmitted-light Dodt gradient images. Laser beam intensity was independently controlled with electro-optical modulators. For some dual recordings, two-photon imaging was used to target a second location following initial somatic or dendritic recording.

Compartmental modeling

Simulations were performed in NEURON 7.5 (Carnevale and Hines, 2006). Our model was based on the model developed in Hay et al. (2011) and later modified in Shai et al. (2015). We employed a simplified morphology that facilitated stretching and scaling as shown in Figure S7. Our ball-and-stick morphology consisted of a cylindrical soma (length and diameter = 30 μm), a 55 μm axon (diameter = 1 μm), and a 500 μm apical dendrite (tapered diameter from 3.5 to 3 μm) that branched into two 200 μm primary tuft dendrites (diameter = 1.89 μm), which each branched into two 100 μm terminal tuft dendrites (diameter = 1.19 μm).

We used the ionic mechanisms from Hay et al. (2011) and Shai et al. (2015), with alterations to suit the new morphology and to match our published (Harnett et al., 2013, 2015) and present experimental results (Table S2). Importantly, previous models failed to recapitulate key aspects of the active behavior of rat TEA L5 neurons, especially the voltage-clamp experiments in Figures 5 and 6. Axial resistance was set to 110 Ω*cm. To account for dendrites and spines not explicitly modeled, membrane capacitance was set higher in the model than measured in Figure S4. Specific membrane capacitance was set to 1 $\mu F/cm^2$ in the axon, 3 $\mu F/cm^2$ in soma, and 2 $\mu F/cm^2$ in the dendrites to match experimental time constants (Figure S1). To model the longer apical arbor of human neurons, we multiplied the y coordinates of each apical dendritic compartment by a factor of 2.5. Two approaches were employed to redistribute ionic conductances (Figures 7 and S7). In the stretched model, the relative position of the conductances was

anchored to the morphology, such that the total conductance (across the entire apical tree) was maintained. In the scaled model, the local conductance densities were maintained, increasing the total conductance of the dendrites.

Current injection and voltage measurements were simulated at the soma and the first bifurcation point (500 μm from the soma in the rat model and 1250 μm from the soma in the stretched and scaled models). Voltage clamp was simulated as a single electrode point process without series resistance. All simulations were conducted at 37°C.

QUANTIFICATION AND STATISTICAL ANALYSIS

Analysis of voltage and current waveforms was performed using custom-written MATLAB codes. Voltage signals were low-pass filtered at 2.5 kHz for outside-out recordings and some whole-cell recordings. Outside-out recordings traces were low-pass filtered at 100 Hz for display in Figure 7. Input resistance was calculated from the slope of the I-V relationship in response to hyperpolarizing current injections. Voltage sag was calculated for current injection of −500 pA as (peak-steady state)/peak. Spike full-width at half-max and area were computed using the base (calculated as the lowest voltage where the first derivative crossed 2 V/s) and the absolute peak of the spike. Effective time constants were calculated from the voltage relaxation following a −100 pA current injection. The fitted region spanned from 0.5 ms after the end of the current pulse until where the voltage relaxed back 75% of the way.

Capacitive transients from nucleated patches were fitted to extract a time constant (tau) with a first order exponential function excluding the first 5 samples (0.025 ms) after the voltage change. The steady-state current (I_{ss}) was computed as the mean current during the last 5 ms of the pulse, while the peak current (I_{peak}) was determined by extrapolating the fit function to the beginning of the current pulse (Gentet et al., 2000). The series resistance (R_s) was calculated as −5 mV / I_{peak} and the patch resistance (R_p) was calculated as (−5 mV / I_{ss}) - R_s. R_p was always above 0.5 GΩ. The patch capacitance (C_p) was calculated as tau*(1/ R_s + 1/ R_p). From two-photon stacks (~0.1 × 0.1 × 0.5 μm resolution), the central (biggest) cross-section was used to compute the major and minor axes of the nucleated patch. The surface area (A) was calculated as (π/4)*(major axis + minor axis)^2. The surface areas for rat and human nucleated patches were 481 ± 12 versus 532 ± 14 μm^2 (*p = 0.01, unpaired t test; rat: n = 28 recordings from 7 rats; human: n = 16 recordings from 1 patient). Finally, the specific membrane capacitance (C_m) was calculated as C_p /A.

Morphological and distance measurements were performed using ImageJ on two-dimensional maximal intensity projections of 1–2 μm Z series collected at the end of the experiment.

Statistical analysis was performed in MATLAB. D'Agostino-Pearson tests were used to assess normality. For normal data, results are presented as mean ± SEM, and ANOVA with Tukey-Kramer multiple comparison or t test were used for statistical analyses. For most skewed datasets, the median as well as the lower and upper quartiles are presented (representing the interquartile range), and Wilcoxon paired test or Wilcoxon rank sum test were used for statistical analysis. Median and 95% confidence intervals obtained with bootstrapping are presented for firing rates and interspike intervals as a function of injected current. For the 50% attenuation distances in Figures 3 and S4, we used bootstrapping to compute confidence intervals on 50% attenuation distances obtained from logistic regression. Statistical details can be found in the figure legends and in the main text. Reported n values can be found in the figure legends and in the results. They include the number of recordings and the number of rats or human patients from which they were obtained.

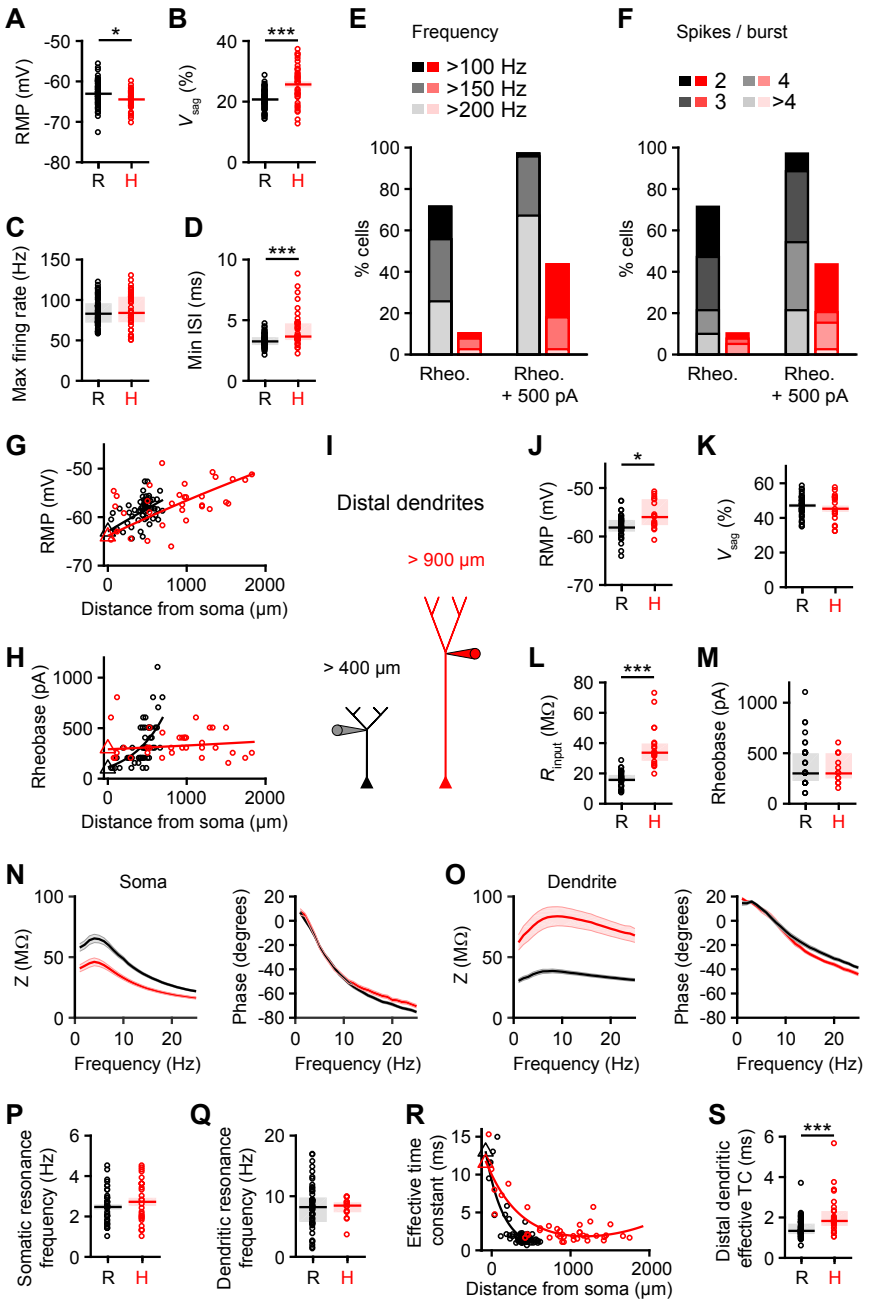

Figure S1. Additional Properties of L5 Neurons, Related to Figures 1 and 2

(A–F) Somatic properties of L5 neurons (rat: n = 70 recordings from 18 rats; human: n = 39 recordings from 6 patients).

(A) Resting membrane potential (*p = 0.01, unpaired t test). Pooled data represent mean ± SEM.

(B) Voltage sag (***$p < 10^{-6}$, unpaired t test). Pooled data represent mean ± SEM.

(C) Maximal steady-state firing rate (p = 0.52, Wilcoxon rank sum test). Pooled data represent median and interquartile range.

(D) Minimum ISI at the best current injection amplitude from Figure 1F (***$p < 10^{-4}$, Wilcoxon rank sum test). Pooled data represent median and interquartile range.

(E) Percentage of cells exhibiting bursts with cut-off frequencies at 100, 150 or 200 Hz.

(F) Percentage of cells exhibiting bursts with 2, 3, 4, or more than 4 APs above 100 Hz.

(G) Resting membrane potential as a function of distance from the soma (rat: n = 88 recordings from 22 rats; human: n = 42 recordings from 7 patients). Triangles are somatic averages and lines are exponential fit to the data.

(H) Rheobase as a function of distance from the soma (rat: n = 57 recordings from 21 rats; human: n = 34 recordings from 7 patients). Triangles are somatic medians and lines are exponential fit to the data.

(I–L) Properties of distal dendrites of L5 neurons (rat: n = 72 recordings from 19 rats; human: n = 26 recordings from 7 patients).

(I) Distance threshold for distal dendrites in rat and human neurons.

(legend continued on next page)

(J) Resting membrane potential (*p = 0.02, Wilcoxon rank sum test). Pooled data represent median and interquartile range.
(K) Voltage sag (p = 0.45, unpaired t test). Pooled data represent mean ± SEM.
(L) Input resistance (***$p < 10^{-12}$, Wilcoxon rank sum test). Pooled data represent median and interquartile range.
(M) Rheobase of distal dendrites (p = 0.93, Wilcoxon rank sum test; rat: n = 43 recordings from 17 rats; human: n = 19 recordings from 4 patients). Pooled data represent median and interquartile range.
(N) Left, impedance profile of rat (black) and human (red) somas in response to sinewaves of 50-100 pA injected at the indicated frequencies for 2 s (rat: n = 41 recordings from 16 rats; human: n = 28 recordings from 5 patients). Right, phase offset between the voltage response and the injected current. Pooled data represent mean ± SEM.
(O) Same as N but for distal dendrites (rat: n = 56 recordings from 17 rats; human: n = 16 recordings from 6 patients).
(P) Somatic resonance frequency for data in N (phase = 0°; p = 0.27, unpaired t test). Pooled data represent mean ± SEM.
(Q) Distal dendritic resonance frequency for data in O (p = 0.91, Wilcoxon rank sum test). Pooled data represent median and interquartile range.
(R) Effective time constant as a function of distance from the soma (rat: n = 88 recordings from 22 rats; human: n = 42 recordings from 7 patients). Triangles are somatic averages and lines are exponential fit to the data.
(S) Effective time constant in distal dendrites (***$p < 10^{-4}$, Wilcoxon rank sum test; rat: n = 72 recordings from 19 rats; human: n = 26 recordings from 7 patients). Pooled data represent median and interquartile range.

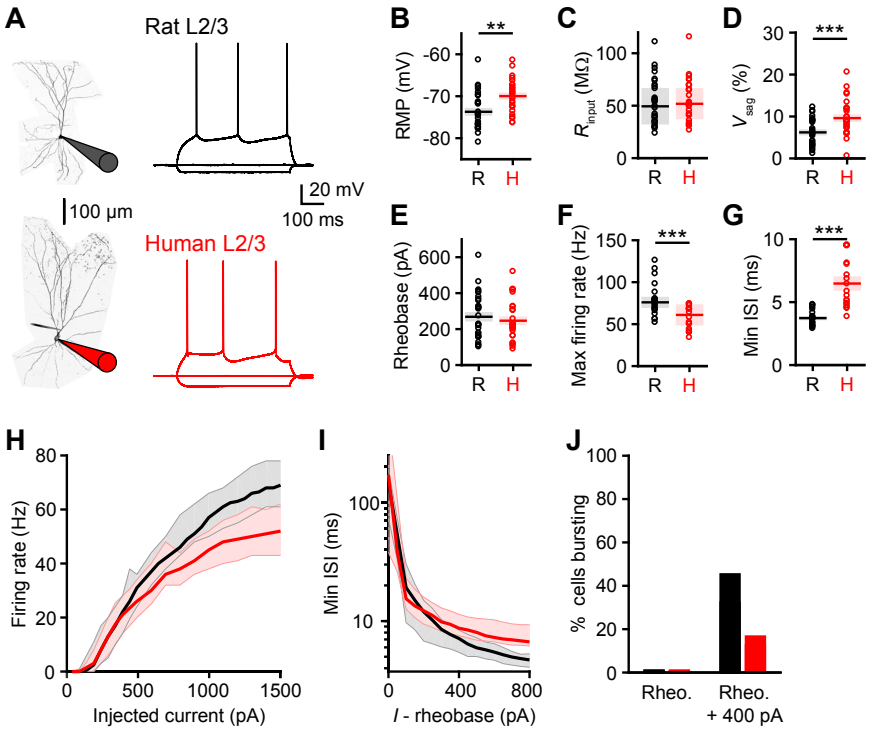

Figure S2. Somatic Properties of L2/3 Neurons, Related to Figure 1

(A) Left, two-photon Z stack montage image of rat (top) and human (bottom) L2/3 neurons with somatic patch-clamp electrodes. Right, rat (black) and human (red) somatic voltage in response to step current injections (−200 pA and rheobase).

(B–E) Subthreshold properties of L2/3 neurons (rat: n = 29 recordings from 8 rats; human: n = 28 recordings from 7 patients).

(B) Resting membrane potential (**p = 0.001, unpaired t test). Pooled data represent mean ± SEM.

(C) Input resistance (p = 0.53, Wilcoxon rank sum test). Pooled data represent median and interquartile range.

(D) Voltage sag (***p = 0.0009, unpaired t test). Pooled data represent mean ± SEM.

(E) Rheobase (p = 0.49, unpaired t test). Pooled data represent mean ± SEM.

(F-J) AP properties of L2/3 neurons (rat: n = 22 recordings from 8 rats; human: n = 18 recordings from 7 patients).

(F) Maximal steady-state firing rate (***p = 0.0004, Wilcoxon rank sum test). Pooled data represent median and interquartile range.

(G) Minimum instantaneous ISI at the best current injection amplitude from (I) (***$p < 10^{-5}$, unpaired t test). Pooled data represent mean ± SEM.

(H) Firing rates as a function of injected current. Population medians with 95% confidence interval error bars are shown.

(I) Minimum instantaneous ISI as a function of injected current above rheobase. Population medians with 95% confidence interval error bars are shown.

(J) Percentage of neurons exhibiting bursts (> 150 Hz) at rheobase and rheobase + 400 pA.

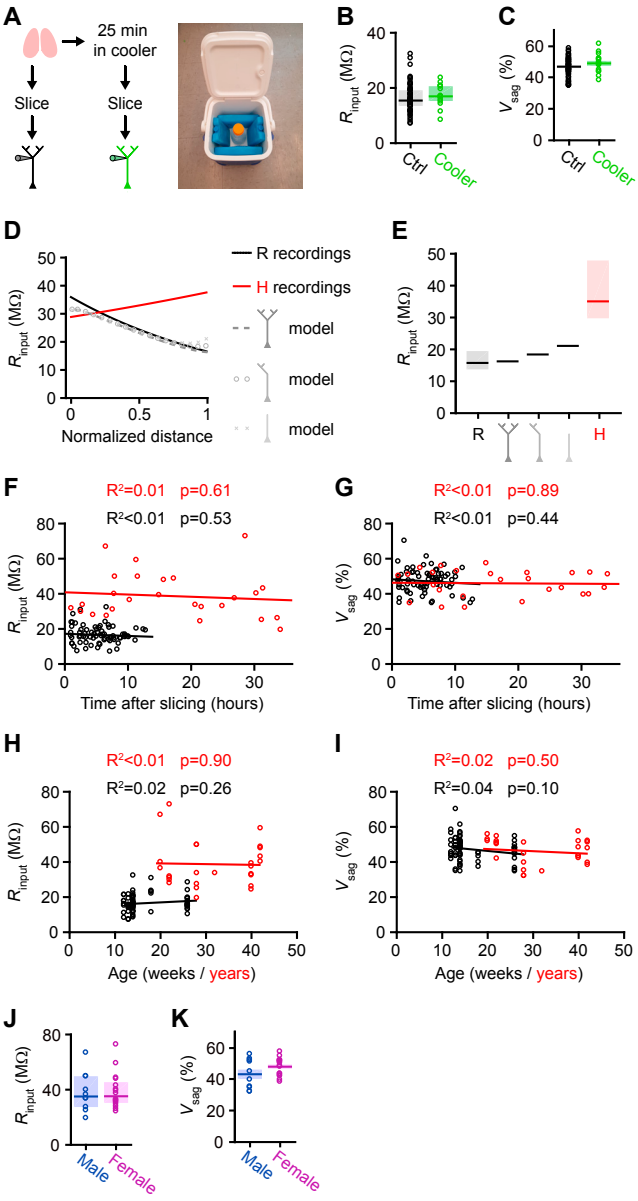

Figure S3. Impact of Methodological Constraints on Dendritic Properties, Related to Figure 2

(A) Control experiment to account for the transport of human brain samples prior to slicing. Rat hemispheres were either sliced right away or after spending 25 minutes in a cooler to mimic the transport of human brain samples.

(B and C) Properties of control and cooler rat distal (> 400 μm from the soma) dendrites (control: n = 57 recordings from 17 rats; cooler: n = 15 recordings from 4 rats).

(B) Input resistance (p = 0.21, Wilcoxon rank sum test). Pooled data represent median and interquartile range.

(C) Voltage sag (p = 0.28, unpaired t test). Pooled data represent mean ± SEM.

(D) Input resistance as a function of distance normalized to the major bifurcation point. Solid lines are fit to experimental rat (black) and human (red) data from Figure 2C. Gray lines represent intact model (dash), partially cut tuft (circle) and fully cut tuft (cross).

(E) Input resistance at the main bifurcation point for experimental rat (left) and human (right) data from Figure S1L and the models (middle) in D.

(F–I) Impact of recording time after slicing or age on distal (> 400 μm and > 900 μm from the soma in rats and humans, respectively) dendritic properties (rat: n = 72 recordings from 19 rats; human: n = 26 recordings from 7 patients). R^2 and p for simple linear regression are indicated above the panels. No significant correlations were observed.

(F) Input resistance as a function of time after slicing.

(G) Voltage sag as a function of time after slicing.

(H) Input resistance as a function of age.

(I) Voltage sag as a function of age.

(legend continued on next page)

(J and K) Properties of distal (> 900 μm from the soma) human dendrites from male and female patients (male: n = 10 recordings from 4 patients; female: n = 16 recordings from 3 patients).
(J) Input resistance ($p > 0.99$, Wilcoxon rank sum test). Pooled data represent median and interquartile range.
(K) Voltage sag ($p = 0.12$, unpaired t test). Pooled data represent mean ± SEM.

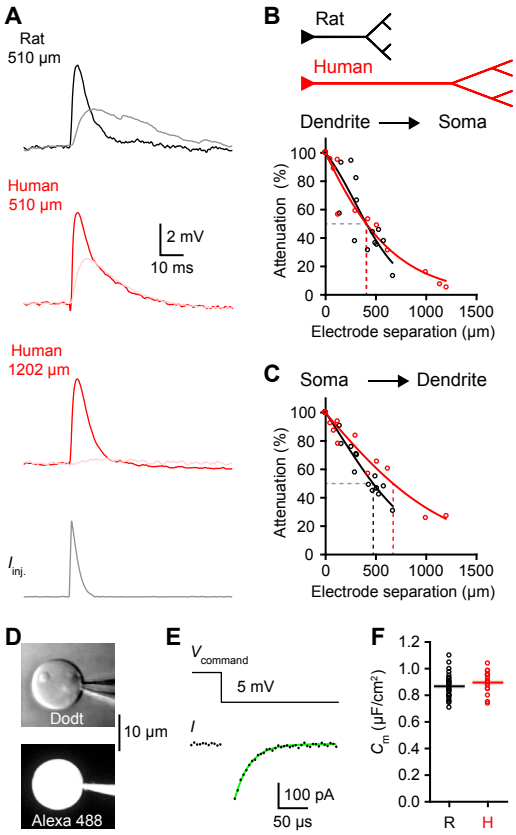

Figure S4. Conserved Specific Membrane Capacitance in Rat and Human Neurons, Related to Figure 3

(A) Distal (black/ red) and proximal (gray/ light red) EPSPs generated through the injection of artificial EPSC (bottom) at the distal site. For a comparable distance, rat and human EPSPs show similar attenuation. Due to their increased length, human dendrites experience more attenuation. EPSC amplitude was adjusted to generate ~5 mV local EPSPs.

(B) Distance-dependent EPSP attenuation toward the soma (rat: n = 13 recordings from 8 rats; human: n = 11 recordings from 2 patients). Lines represent logistic fit to the data. Dashed lines represent 50% attenuation.

(C) Distance-dependent EPSP attenuation toward the dendrites (rat: n = 14 recordings from 9 rats; human: n = 10 recordings from 2 patients).

(D) Two-photon stack of a human L5 nucleated patch. Top, Dodt image. Bottom, Alexa 488 injected through the pipette.

(E) Voltage-clamp 5 mV step (top) and capacitive transient (bottom). The green line represents an exponential fit to the decay.

(F) Specific membrane capacitance of rat and human L5 neurons (0.87 ± 0.02 versus 0.90 ± 0.02 µF/cm^2; p = 0.32, unpaired t test; rat: n = 28 recordings from 7 rats; human: n = 16 recordings from 1 patient). Pooled data represent mean ± SEM.

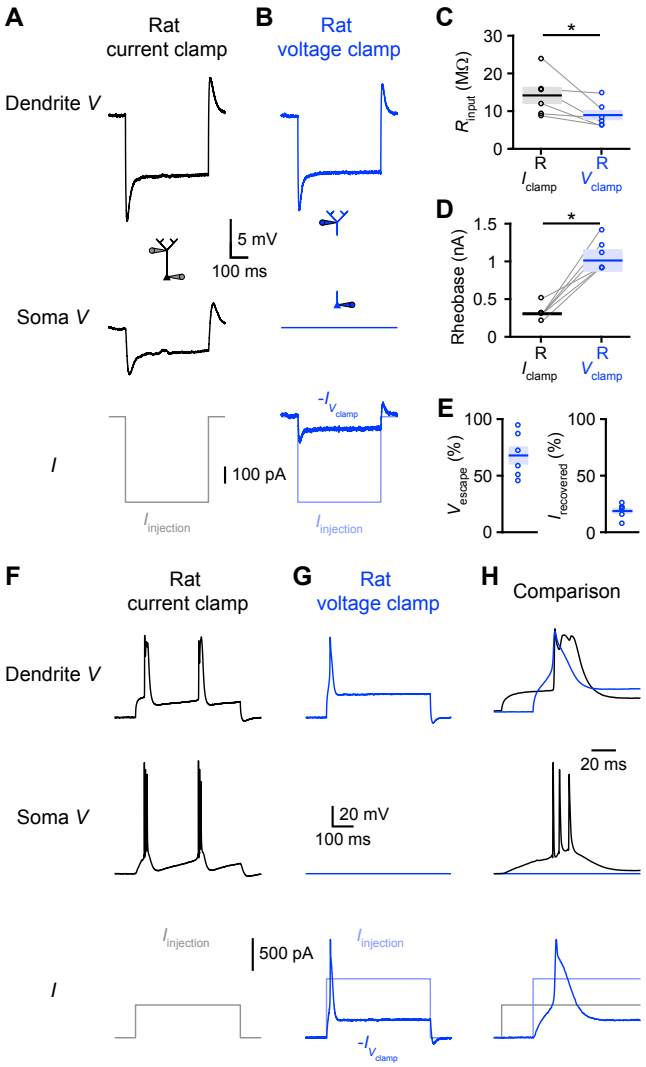

Figure S5. Rat Dendritic Properties under Somatic Voltage Clamp, Related to Figure 5

(A) Under control conditions, a hyperpolarizing dendritic step current injection (bottom; 500 pA) elicits a dendritic voltage response (top) that attenuates toward the soma (middle).

(B) Under somatic voltage clamp (middle), the same current injection as in A (bottom) elicits a dendritic voltage response (top) that escapes from the somatic voltage clamp. The voltage clamp recovers a small fraction of the injected current (bottom).

(C) Dendritic input resistance under somatic current clamp and voltage clamp (*p = 0.04, paired t test; n = 6 recordings from 5 rats). Pooled data represent mean ± SEM.

(D) Dendritic rheobase under somatic current clamp and voltage clamp (*p = 0.03, Wilcoxon paired test; n = 6 recordings from 5 rats). Pooled data represent median and interquartile range.

(E) Percentage of steady-state voltage escape (left) and recovered current (right) for hyperpolarizing 500 pA step current injection (n = 6 recordings from 5 rats). Pooled data represent mean ± SEM.

(F) Under control conditions, rheobase current injection (bottom) into the dendrite elicits dendritic spikes (top) associated with somatic bursts (middle).

(G) Under somatic voltage clamp (middle), rheobase current injection (bottom) into the dendrite elicits a weaker dendritic spike (top). The voltage clamp recovers current with similar kinetics as the dendritic spike (bottom).

(H) Comparison of dendritic and somatic voltage waveforms from F and G.

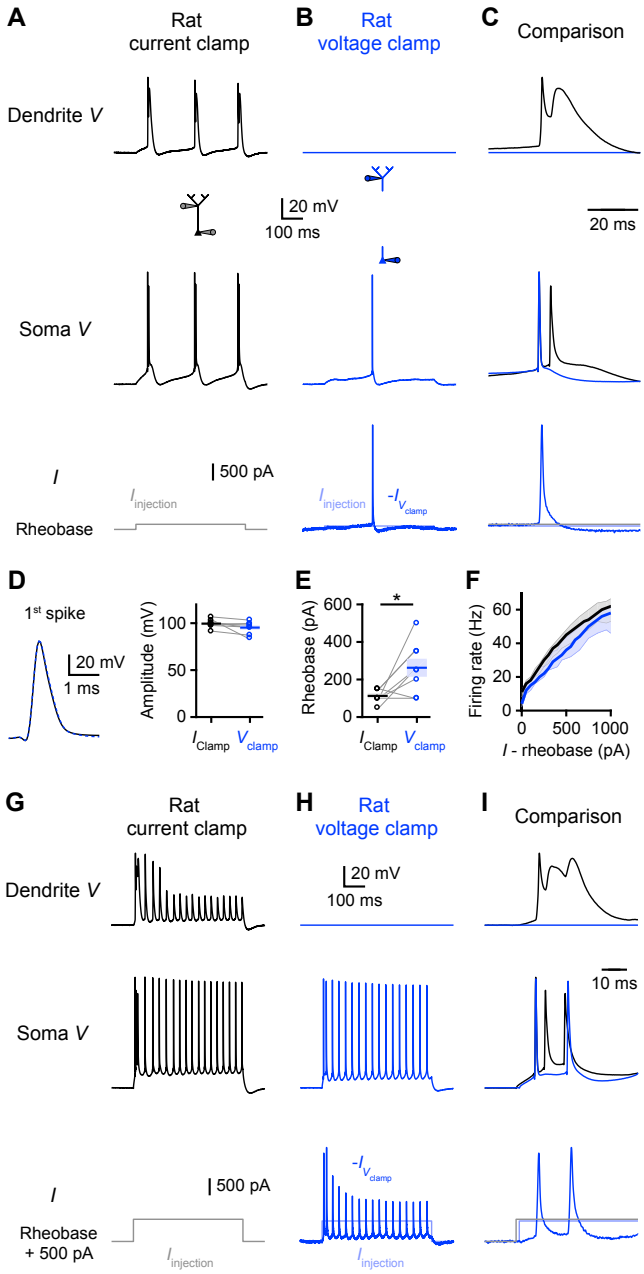

Figure S6. Rat Somatic Burst Properties under Dendritic Voltage Clamp, Related to Figure 6

(A–C) The impact of dendritic voltage clamp on somatic burst firing at rheobase.

(A) Under control conditions, rheobase current injection (bottom) into the soma elicits somatic bursts (middle) associated with dendritic spikes (top).

(B) Under dendritic voltage clamp (top), rheobase current injection (bottom) into the soma elicits a single somatic AP (middle). The voltage clamp records a large transient associated with the backpropagating AP (bottom).

(C) Comparison of dendritic and somatic voltage waveforms from A and B. The first somatic AP is identical under the two conditions but dendritic voltage clamp eliminates the dendritic spike and the second somatic AP.

(D) First somatic AP waveform for both conditions. Dendritic voltage clamp did not significantly reduce the amplitude of the first AP (99.8 ± 1.6 versus 95.6 mV ± 2.3, p = 0.10, paired t test; n = 8 recordings from 5 rats). Pooled data represent mean ± SEM.

(E) Rheobase under current clamp and voltage clamp (*p = 0.02, paired t test; n = 8 recordings from 5 rats). Pooled data represent mean ± SEM.

(F) Firing rates as a function of injected current above rheobase (n = 8 recordings from 5 rats). Population medians with 95% confidence interval error bars are shown.

(G–I) The impact of dendritic voltage clamp on somatic bursting at rheobase + 500 pA.

(G) Under control conditions, suprathreshold (rheobase + 500 pA) current injection (bottom) into the soma elicits an initial somatic burst (middle) associated with a dendritic spike (top).

(legend continued on next page)

(H) Under dendritic voltage clamp (top), suprathreshold current injection (bottom) into the soma elicits multiple somatic APs (middle) without bursting. The voltage clamp records large transients (bottom) associated with the backpropagating APs.
(I) Comparison of dendritic and somatic voltage waveforms from G and H. Dendritic voltage clamp prevents the recruitment of dendritic voltage-gated channels causing the dendritic spike and somatic burst.

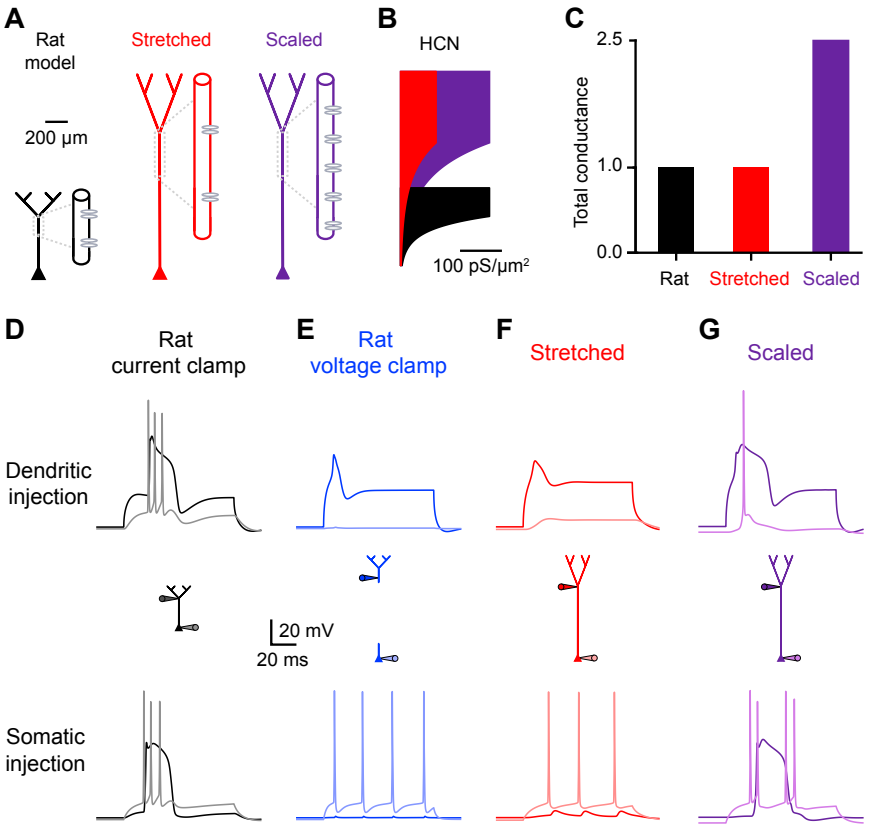

Figure S7. Stretched and Scaled Biophysical Models, Related to Figure 7

(A) Left, rat model with schematic density of ion channels in a dendritic segment. Middle, stretched model where the apical dendrites are lengthened without affecting the total number of ion channels. Right, scaled model where the apical dendrites are lengthened and ion channels are added to maintain the local ion channel density.

(B) Distance-dependent rat (black), stretched (red), and scaled (purple) distribution of HCN channels.

(C) Total conductance in the apical dendrite for the three models, normalized to the rat model.

(D–G) Comparison of dendritic and somatic voltage waveforms in the different models during threshold dendritic (top) or somatic (bottom) current injections.

(D) Rat model with dendritic voltage in black and somatic voltage in gray. Top, the threshold dendritic spike is associated with a somatic burst. Bottom, high-frequency APs are coupled to dendritic spikes.

(E) Rat model under somatic (top) or dendritic (bottom) voltage clamp with dendritic voltage in blue and somatic voltage in light blue. Top, the threshold dendritic spike is weaker than in D. Bottom, low-frequency APs.

(F) Stretched model with dendritic voltage in red and somatic voltage in light red. Top, the threshold dendritic spike fails to elicit somatic AP. Bottom, low-frequency somatic APs fail to engage distal dendrites.

(G) Scaled model with dendritic voltage in purple and somatic voltage in light purple. Top, the threshold dendritic spike triggers somatic APs. Bottom, somatic APs engage distal dendritic electrogenesis.